Article:
Milletari, Mirco and Ferreira, Aires orcid.org/0000-0001-6017-8669 (2016) Quantum Diagrammatic Theory of the Extrinsic Spin Hall Effect in Graphene. Physical Review B. 134202. ISSN 2469-9969

https://doi.org/10.1103/PhysRevB.94.134202

Quantum diagrammatic theory of the extrinsic spin Hall effect in graphene

Mirco Milletarì*
Centre for Advanced 2D Materials and Department of Physics, National University of Singapore, Singapore, 117551

Aires Ferreira†
Department of Physics, University of York, York YO10 5DD, United Kingdom
(Received 12 April 2016; published 11 October 2016)

We present a rigorous microscopic theory of the extrinsic spin Hall effect in disordered graphene based on a nonperturbative quantum diagrammatic treatment incorporating skew scattering and *anomalous* (impurity-concentration-independent) quantum corrections on equal footing. The leading skew-scattering contribution to the spin Hall conductivity is shown to quantitatively agree with Boltzmann transport theory over a wide range of parameters. Our self-consistent approach, where all topologically equivalent noncrossing diagrams are resummed, unveils that the skewness generated by spin-orbit-active impurities deeply influences the anomalous component of the spin Hall conductivity, even in the weak-scattering regime. This seemingly counterintuitive result is explained by the rich sublattice structure of scattering potentials in graphene, for which traditional Gaussian disorder approximations fail to capture the intricate correlations between skew scattering and side jumps generated through diffusion. Finally, we assess the role of quantum interference corrections by evaluating an important subclass of crossing diagrams recently considered in the context of the anomalous Hall effect, the X and Ψ diagrams [A. Ado *et al.*, Europhys. Lett. **111**, 37004 (2015)]. We show that Ψ diagrams, encoding quantum coherent skew scattering, display a strong Fermi energy dependence, dominating the anomalous spin Hall component away from the Dirac point. Our findings have direct implications for nonlocal transport experiments in spin-orbit-coupled graphene systems.

DOI: 10.1103/PhysRevB.94.134202

I. INTRODUCTION

Spin Hall effects, the collection of transport phenomena whereby charge currents propagating in nonmagnetic materials are converted to transverse spin currents and vice versa [1–3], constitute a rapidly evolving front of spintronics research. Following their first demonstrations in semiconductors and metals [4,5], spin Hall effects (SHEs) have been explored to devise novel schemes for interconversion of spin and charge signals. In particular, spin-orbit torques induced by the SHE from heavy metals have been explored to manipulate the magnetization dynamics in ferromagnet-metal bilayers, including tuning of spin relaxation and spin-torque switching of the magnetized layer [6–8]. Conversely, the inverse SHE [5] enables the transformation of pure spin currents injected by spin pumping from precessing ferromagnets into electric signals [9]. Spin-orbit interactions are also of paramount importance in the emergent field of "spin caloritronics," where the inverse SHE is utilized to detect spin currents generated by the spin Seebeck effect [10].

The SHE efficiency of a material is characterized by the spin Hall angle, defined as the ratio of z-polarized transverse spin current to longitudinal charge-current densities in the steady state, $\gamma = \mathcal{J}_\perp / J_\parallel$ (see schematic in Fig. 1). In time-reversal-invariant systems, Onsager reciprocity relations dictate that the strengths for the direct and inverse SHEs are the same, and hence γ is an important figure of merit for applications exploring relativistic spin-orbit-coupling phenomena. Since the SHEs have their origin in the coupling between spin and orbital degrees of freedom, clean metals with large spin-orbit coupling [11] and disordered metals with impurity resonances split by the spin-orbit interaction [12] can display robust SHEs, with γ in the range 0.01–0.1.

The impurity-generated extrinsic SHE is of particular interest from both applied and fundamental perspectives. In the presence of local spin-orbit interactions, up and down spin components of wave packets are preferably scattered in opposite directions (skew scattering), leading to the establishment of net spin Hall currents. The degree of skewness, and thus the resulting spin Hall angles, can be modified by varying the impurity concentration or by taking different combinations of host and impurity systems [12,13]. This allows to optimize metallic thin films for usage in spin-current generation (direct SHE) and detection (inverse SHE) schemes. Another appealing scenario is the *in situ* tuning of spin Hall angles for low-power spintronics schemes based on *pure* (charge-neutral) spin currents. The latter is a formidable task that requires the ability to route pure spin currents by means of external gates. A promising candidate is the robust extrinsic SHE predicted to occur in graphene with dilute spin-orbit-active scattering centers [14]. One can envisage that in the vicinity of a sharp impurity resonance, the spin Hall angle would undergo major changes upon tuning of the chemical potential, enabling the reversal of the sign of spin currents. The reversible manipulation of charge transport properties through electrical control of impurity resonances has recently been reported in dual-gated fluorinated bilayer graphene devices [15], suggesting that similar setups could be explored to achieve gate-tunable spin currents in graphene.

An interesting feature of two-dimensional materials is the possibility to introduce spin-orbit coupling (SOC) with different symmetries [16,17] and varying spatial extent

*milletari@gmail.com
†aires.ferreira@york.ac.uk

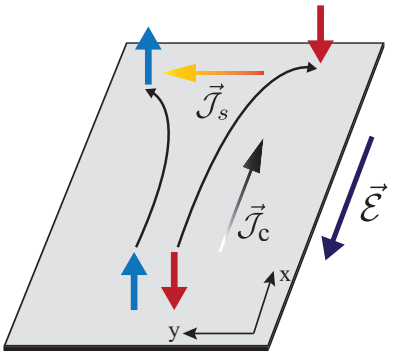

FIG. 1. Schematic of the SHE in a two-dimensional material. An external electrical field drives a charge and spin Hall currents. The reduced dimensionality defines Oz as a preferred spin direction [2].

(subnanometer range using adatoms [18], nanometer scale using clusters [19], and spatially uniform SOC through proximity effect to suitable substrates [20–22]). The important role played by the SOC symmetry in the resonant scattering regime has been elucidated by recent theoretical studies [17,23]. The suitability of graphene for all-electrical spintronics is further supported by recent experimental reports on nonlocal transport in adatom-decorated graphene in Refs. [18,19] and, more recently, on spin pumping in graphene from a magnetic insulator substrate [24]. We finally note that the negligible intrinsic spin-orbit coupling in the band structure of graphene [25,26] is particularly advantageous, as spin Hall currents generated from impurities can propagate large distances without suffering from additional spin relaxation [14].

These recent developments in graphene spintronics motivated us to further investigate the microscopic mechanisms underlying the SHE in models of two-dimensional (2D) massless Dirac fermions subject to spin-orbit interactions. The giant extrinsic SHE proposed in Ref. [14] has its origin in the resonant scattering mechanism ubiquitous in disordered 2D massless Dirac fermions [27–30]. Broadly speaking, the vanishingly small density of states of bare graphene, $\nu(\epsilon) \propto \epsilon$, favors the appearance of sharp impurity resonances and, consequently, large scattering skewness in the presence of SOC. The full conductivity tensor in the charge and spin sectors, including charge-spin transverse (Hall) conductivities, can be conveniently computed by means of Boltzmann transport theory upon careful identification of the transport lifetimes determining asymmetric distortions of the Fermi surface induced by the SOC [14]. The simple semiclassical approach is justified well inside the dilute limit, where skew scattering provides the leading contribution to the spin Hall conductivity, i.e., $\sigma_{\rm SH} = \mathcal{S}(\epsilon)n^{-1}$, where $n \ll 1$ is the SOC-active impurity concentration and $\mathcal{S}(\epsilon)$ is some nonuniversal function of the Fermi energy and microscopic parameters of the model. On the other hand, for not too dilute concentrations (e.g., in the range 0.01%–0.1% atomic ratio) other extrinsic mechanisms can compete with skew scattering [31]. In particular, the trajectory of charge carriers can undergo a transverse spin-dependent displacement upon scattering from a spin-orbit-coupled impurity, the so-called quantum side jump, which gives rise to a net contribution to the spin Hall current. The latter shows up in the next leading term in the spin Hall conductivity expansion,

$$\sigma_{\rm SH} = \mathcal{S}(\epsilon)n^{-1} + \mathcal{Q}(\epsilon) + \cdots , \tag{1}$$

here referred to as the *anomalous* contribution. The determination of the quantum side-jump contribution to $\mathcal{Q}(\epsilon)$ within semiclassical transport theory has been the cause of much debate. Historically, this controversy originated in the closely related anomalous Hall effect (AHE), taking place in ferromagnetic materials [32]. The controversy surrounding the semiclassical description of the side-jump mechanism originated in its association with the Berry connection, which is a gauge-dependent quantity. Recently, a semiclassical formulation preserving $U(1)$ gauge invariance has been developed by Sinitsyn and coworkers [33], which provides a rigorous treatment of quantum-side jump (QSJ) contributions to the AHE in the weak-scattering limit. The quantum linear-response theory and the quasiclassical Keldysh approach [34] provide powerful alternatives to semiclassical approaches. In this paper, we will use the linear-response theory (LRT), where different contributions to the spin Hall (SH) conductivity can be evaluated systematically by means of the diagrammatic technique. Whereas previous use of diagrammatic expansions in studies of the SHE/AHE has traditionally assumed weak-disorder (Gaussian) approximations, a proper treatment of the skew-scattering mechanism in graphene necessarily requires a nonperturbative approach. The most pressing question is how to treat semiclassical skew scattering $\mathcal{S}$ and anomalous quantum scattering $\mathcal{Q}$ processes on equal footing when scattering potentials are no longer weak or exhibit a rich structure, e.g., breaking pseudospin rotational invariance through a mass term [31]. These questions are of much interest in graphene, where spin-orbit-active impurities generally have a complex pseudospin texture [17,35]. Another important related question is the role of quantum coherent contributions in the extrinsic SHE, which remains largely unexplored.

In this paper, we tackle the aforementioned issues by means of a simple, yet powerful, extension of the standard diagrammatic approach originally developed by Baym in the context of the quantum kinetic equation (Kadanoff-Baym) formalism [36]. We show that a proper evaluation of vertex corrections allows us to take into account skew scattering and quantum processes at *all orders* in perturbation theory by means of exact resummations. We find that while the single-impurity (semiclassical) skew-scattering contribution *quantitatively* agrees with Boltzmann theory, the anomalous component of $\sigma_{\rm SH}$ shows a richer structure, with several contributions beyond the semiclassical QSJ processes. One of our main results concerns the role of quantum interference: coherent skew scattering from two impurities is found to provide a remarkably large contribution to $\mathcal{Q}$, opening doors to the observation of quantum coherent processes in nonlocal transport experiments.

This paper is organized as follows. In Sec. II, we set the notation and outline the extended LRT formalism employed in the reminder of the paper. In this section, we also comment on the different types of approximations commonly employed in theoretical studies of AHE/SHE. Section III introduces the disordered spin-orbit-coupled graphene model system under examination, and Sec. IV presents the calculation of the SH conductivity within the weak-scattering regime. The

scope of this section is to highlight the shortcomings of the widely used white-noise Gaussian disorder assumptions. In Sec. V we compare the simple Gaussian result with the full T-matrix calculation and show that the former misses an important Fermi energy dependence. Furthermore, we show that the (semiclassical) skew-scattering contribution within the extended LRT formalism *quantitatively* agrees with the exact solution of the corresponding linearized Boltzmann transport equations. Finally, in Sec. VI we improve upon the noncrossing approximation to incorporate important coherent multiple-scattering contributions. The latter is motivated by recent findings on the importance of a subclass of crossing diagrams for a correct description of the AHE in 2D systems of massive Dirac fermions [37]. By comparing the Gaussian result with the extended LRT based on the T-matrix approach, we will show that the former leads to an incorrect quantitative (and qualitative) picture. More specifically, we show that the Gaussian approximation erroneously predicts the vanishing of a specific set of crossing diagrams (Ψ diagrams). Indeed, our self-consistent treatment shows that these diagrams give a dominant contribution in some regions of the parameter space, demonstrating again the limitations of the Gaussian approximation.

II. METHODOLOGY

In this paper we are interested in models of disordered graphene where the out-of-plane spin polarization is conserved (see Sec. III). In such models, the charge- and spin-current density operators are given by the standard expressions [38]

$$\mathbf{J} = -e\,\Psi^{\dagger}(\mathbf{x})\,\mathbf{v}\,\Psi(\mathbf{x}), \tag{2}$$

$$\mathcal{J} = -e\,\Psi^{\dagger}(\mathbf{x})\,\tfrac{1}{2}\{s_z,\mathbf{v}\}\,\Psi(\mathbf{x}), \tag{3}$$

respectively. Here, $\{\cdot,\cdot\}$ denotes the anticommutator, $\mathbf{v}$ is the velocity operator, $-e<0$ is the electron's charge, and $s_z \equiv s_3$ is the diagonal Pauli matrix with eigenvalues ± 1. The spin-charge conductivity tensor describing the interconversion of charge and spin currents in the presence of SOC is given by the Kubo-Streda formula [39]

$$\sigma^{z}_{ij} = \frac{\hbar}{2\pi\Omega}\mathrm{Tr}\langle J_i(G^R-G^A)\mathcal{J}_j G^A - \mathcal{J}_j(G^R-G^A)J_i G^R\rangle_{\mathrm{dis}}, \tag{4}$$

where

$$G^{R(A)} = \frac{1}{\epsilon - H_0 - V \pm i0^{+}} \tag{5}$$

is the retarded (advanced) Green's function associated with the total Hamiltonian, $H = H_0 + V$, with H_0 denoting the bare term and V being the disorder potential from impurities located at random positions $\{\mathbf{x}_i\}$. The terms J_i and $\mathcal{J}_j$ are Cartesian components of the charge- and spin-current density operator, respectively, and $\langle\cdots\rangle_{\mathrm{dis}}$ denotes the disorder configurational average according to the standard prescription

$$\langle O\rangle_{\mathrm{dis}} = \lim_{N,\Omega\to\infty}\left(\prod_{i=1}^{N}\int_{\Omega}\frac{d^2x_i}{\Omega}\right)O(\mathbf{x}_1,\ldots,\mathbf{x}_N)\Big|_{\frac{N}{\Omega}=n}, \tag{6}$$

where i labels the impurities and Ω is the area of the sample. Finally, Tr denotes the trace over the complete Hilbert space.

Owing to time-reversal symmetry, the off-diagonal entries of the tensor σ^{z}_{ij} $(i\neq j)$ characterize both the transverse spin-current density generated by a longitudinal electric field, $\mathcal{J}_i = \sigma^{z}_{ij}\mathcal{E}^{z}_{j}$, and the transverse charge-current density induced by a spin-dependent chemical-potential gradient, $J_i = \sigma^{z}_{ij}\mathcal{E}^{z}_{j}$. Note that the charge-spin tensor is antisymmetric with respect to the exchange of direction indexes, $\sigma^{z}_{ij} = -\sigma^{z}_{ji}$. In what follows, we define $\sigma_{\mathrm{SH}} \equiv \sigma^{z}_{yx}$. We also make use of natural units $\hbar \equiv 1 \equiv e$ (the units are restored in the final expressions for the SH conductivity).

The terms in Eq. (4) involving the product of two Green's functions in the same sector contribute only at order n, and therefore can be safely neglected (see Sec. IV for details). The SH conductivity then reduces to

$$\sigma_{\mathrm{SH}} = \frac{1}{\pi\Omega}\mathrm{Tr}\,[\langle G^R J_x G^A\rangle_{\mathrm{dis}}\mathcal{J}_y], \tag{7}$$

where we used the fact that in Dirac theories, extrinsic SOC does not generate additional terms in the velocity operator. This allows us to bring one of the current operators outside the configurational average. The SH conductivity [Eq. (7)] can be evaluated by means of standard diagrammatic techniques for disordered electrons [40]. Studies of the SHE traditionally evaluate a selection of low-order diagrams encoding scattering processes in the weak-perturbation regime. As explained in the Introduction, the latter approach is not generally suitable for 2D massless Dirac fermions, where perturbations induced by impurities can be quite strong. For this reason, we follow the approach originally developed by Baym [36] in the quantum kinetic equation formalism, which enables a self-consistent evaluation of the conductivity tensor at the full T-matrix level. The extended formalism has been applied in Ref. [41] to study resonant impurity scattering in anisotropic superconductors. In this approach, one introduces disorder-averaged Green's functions

$$\mathcal{G}^{\lambda} = \frac{1}{\left(G^{\lambda}_0\right)^{-1} - \Sigma^{\lambda}}, \tag{8}$$

where G^{λ}_0 denotes the Green's function of the unperturbed system, $\lambda = \{R,A\}$ specifies retarded and advanced sectors, and $\Sigma^{\lambda} = \langle V + VG^{\lambda}_0V + \cdots\rangle_{\mathrm{dis}}$ is the self-energy. Assuming a short-range potential of the form $V = \sum_i W(\mathbf{x}-\mathbf{x}_i)$, the latter can be written as

$$\Sigma^{\lambda} = n\,T^{\lambda} + \delta\Sigma^{\lambda}, \tag{9}$$

where

$$T^{\lambda} = W\frac{1}{1-G^{\lambda}_0 W} \tag{10}$$

is the average T matrix describing scattering off a single impurity and $\delta\Sigma^{\lambda}$ contains $O(n^2)$ terms. Here, $\delta\Sigma^{\lambda}$ contains two physically different classes of diagrams that are higher order in the impurity density n: those with crossing impurity lines and those without. The former describe coherent scattering processes off multiple impurities, while the latter describe uncorrelated processes taking place at higher impurity density. For this reason, terms without crossing impurity lines can be easily included in the T matrix in a self-consistent way

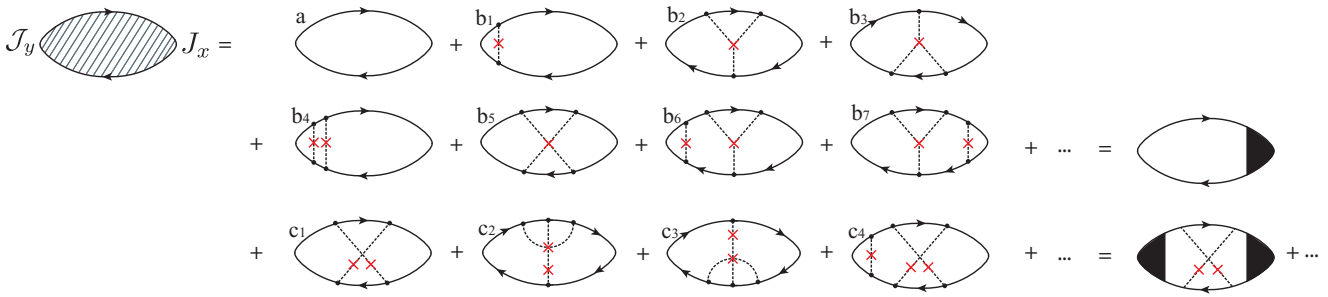

FIG. 2. Feynman diagrams considered in this work. (a) is the empty bubble, and the remaining diagrams encode vertex corrections. The set $\{b_i\}_{i=1...\infty}$ is the complete series of noncrossing two-particle diagrams, which contain the conventional ladder diagrams as a subset $\{b_1, b_4, \dots\}$. The last line shows crossing diagrams obtained when the full T matrix $\mathcal{T}^\lambda$ is used [Eq. (11)]. Thick black lines represent disorder-averaged propagators, dashed black lines represent potential W insertions, and the crosses represent impurity-density insertions.

[40]. On the other hand, crossing diagrams are not, in general, easy to resum; however, these diagrams are associated with an extra factor of smallness of the order of $(k_F\, l)^{-1}$, where k_F is the Fermi momentum and l is the mean free path. For this reason, crossing diagrams can be ignored in the semiclassical limit $k_F l \gg 1$. Under disorder average and neglecting crossing diagrams in the self-energy, one can recast Eq. (7) into the convenient form

$$\sigma_{\rm SH} = \frac{1}{\pi\Omega}{\rm Tr}[\mathcal{G}^R\, J_x\, \mathcal{G}^A\, \mathcal{J}_y] + \frac{1}{\pi\Omega}{\rm Tr}[\mathcal{G}^A \mathcal{J}_y \mathcal{G}^R \langle \mathcal{T}^R \mathcal{G}^R J_x \mathcal{G}^A \mathcal{T}^A\rangle_{\rm dis}], \qquad (11)$$

with $\mathcal{T}^\lambda$ defined by the relation $\mathcal{T}^\lambda = V + V\,\mathcal{G}^\lambda\,\mathcal{T}^\lambda$. The first line provides the "empty-bubble" contribution to the SH conductivity (diagram a in Fig. 2), and the second line describes the so-called vertex corrections. While the self-energy dresses the bare propagator (two-point function) in Eq. (8), the second line of Eq. (11) encodes the dressing of the response function (four-point function), represented diagrammatically by two-particle noncrossing and crossing diagrams, b_i and c_i, respectively, in Fig. 2.

The two-particle noncrossing diagrams ($\{b_i\}$) contain information about the standard semiclassical skew scattering and QSJ: two parametrically distinguishable contributions with their origin in incoherent (single-impurity) scattering. Formally, the resummation of this class of diagrams is performed substituting $\mathcal{T}^\lambda$ in Eq. (11) by its disorder average, that is, $\mathcal{T}^\lambda \to T^\lambda$. It is worth noting that the Born approximation $T^\lambda \approx V$ leads to the familiar ladder diagrams b_1, b_4, ... in Fig. 2. The resummation of the Born ladder series yields the commonly employed approximation to the QSJ [39,42–45]. However, by keeping the full T-matrix structure one effectively resums all topologically equivalent, two-particle noncrossing diagrams at all orders in V. The additional terms generated by the T-matrix insertions encompass not only skew scattering from arbitrarily strong potentials but also important corrections to the anomalous term in Eq. (1) (see Secs. IV and V A for details).

Finally, the two-particle crossing diagrams ($\{c_i\}$) contain quantum corrections arising from coherent multiple scattering from two or more impurities. Similar to weak-localization corrections to the longitudinal conductivity, these diagrams come with an extra factor of smallness $(k_F\, l)^{-1}$ due to the crossing of lines belonging to different impurity-density insertions. For this reason, it was believed that their effect would be relevant only in the deep quantum regime, $k_F\, l \ll 1$. However, this argument is not generally correct, as c_i diagrams with two impurity crossing lines also contribute to order $(k_F\, l)^0$ in the transverse conductivity, and therefore correct $\mathcal{Q}(\epsilon)$ in Eq. (1). This was recently discovered by Ado *et al.* [37] in the context of the AHE with massive Dirac fermions. As shown in Sec. VI for our model, the crossing diagrams encoding quantum coherent skew scattering off two impurities provide the dominant anomalous contribution over a wide range of parameters, attaining remarkably large values away from the Gaussian regime.

III. MODEL SYSTEM

As a model system we consider a graphene sheet with extrinsic SOC with its origin in spin-orbit-active impurities. The low-energy physics is captured by a Dirac Hamiltonian in two spatial dimensions with a random impurity potential. It is convenient to introduce the SO(5) representation of the spin algebra [46,47] in terms of $4 \times 4 = 1 + 5 + 10$ matrices, i.e., one identity, γ^0; five γ^a matrices, taken as $\gamma^1 = \sigma_1 \otimes s_0$, $\gamma^2 = \sigma_2 \otimes s_0$, $\gamma^3 = \sigma_3 \otimes s_3$, $\gamma^4 = \sigma_3 \otimes s_2$, and $\gamma^5 = \sigma_3 \otimes s_1$; and ten adjoint matrices, $\gamma^{ab} = i/2\,[\gamma^a, \gamma^b]$, where $\boldsymbol{\sigma}$ and $\boldsymbol{s}$ are Pauli matrices defined in the sublattice and spin space, respectively. The Hamiltonian density around the K valley is given by

$$\mathscr{H} = \psi^\dagger(\mathbf{x})\{-i\, v\, \gamma^j \partial_j - \gamma_0\, \epsilon + V(\mathbf{x})\}\psi(\mathbf{x}), \qquad (12)$$

where v is the Fermi velocity of charge carriers, ϵ is the Fermi energy, and $V(\mathbf{x})$ denotes the disorder potential. In this paper, we consider short-range impurity potentials of the form

$$V(\mathbf{x}) = \sum_{i=1}^{N} M\, R^2 \delta(\mathbf{x} - \mathbf{x}_i), \qquad (13)$$

where M is a 4×4 matrix encoding the spin and sublattice texture of the impurity and R is a length scale mimicking a potential range [30]. We note that, generally speaking, impurity potentials in the continuum limit are described by enlarged 8×8 matrices accounting for the valley degree of freedom. In fact, when the impurity range is of the order of the lattice spacing, intervalley processes can counteract the intravalley skew scattering, leading to an overall reduction of the SH

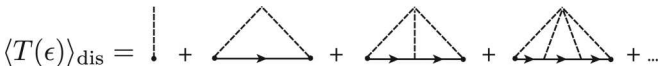

FIG. 3. T-matrix expansion. The truncated series of diagrams constituting the T matrix is shown up to fourth order in the impurity potential (black dots). The continuum lines are bare propagators.

conductivity [17]. In the current work, we avoid additional complications arising from intervalley scattering and limit the discussion to the simplest model displaying SHE. We therefore consider scattering potentials with "intrinsic-type" ($\sigma_3 s_3$) SOC [25,26],

$$M = \alpha_0\,\gamma_0 + \alpha_3\,\gamma_3, \tag{14}$$

where α_3 (α_0) is the SOC (electrostatic potential) magnitude. The intrinsic-type SOC conserves the out-of-plane spin component in addition to being an invariant of the C_{6v} point group, and thus it is the simplest form of SOC in graphene; physical realizations include physisorbed atoms in the hollow position and randomly distributed top-position adatoms forming small clusters [17]. The presence of two different terms in the scattering potential is responsible for a rich phenomenology, most noticeably a crossover between skew-scattering- and QSJ-dominated SHEs in experimentally accessible parameter regions, as demonstrated by the authors in Ref. [31]. In the following sections, we also show that the simultaneous presence of two energy scales associated with the impurities leads to the breakdown of commonly employed approximations.

Being interested in the effect of asymmetric and strong scattering, we show that the standard Gaussian *white-noise* approximation is not generally valid. In fact, as we show in Sec. IV, the Gaussian approximation results in an ϵ-independent anomalous contribution $\mathcal{Q}$. To correctly take into account the role of the Fermi energy, we employ the T-matrix approach introduced in Sec. II. Within this approach, the self-energy reads $\Sigma(\epsilon) = n\,\langle T(\epsilon)\rangle_{\rm dis}$, with the averaged T matrix formally given by Eq. (10); its diagrammatic representation is given in Fig. 3. We find after some straightforward algebra

$$\langle T(\epsilon)\rangle_{\rm dis} = \tfrac{1}{2}(T_+ + T_-)\gamma_0 + \tfrac{1}{2}(T_+ - T_-)\gamma_3 \equiv T, \tag{15}$$

with

$$T_\pm = \frac{R^2\,(\alpha_0 \pm \alpha_3)}{1 - R^2\,(\alpha_0 \pm \alpha_3)\,g_0(\epsilon)} \equiv \epsilon_\pm \mp i\,\eta_\pm. \tag{16}$$

In the above, $g_0(\epsilon) = -\epsilon/2\pi v^2 \ln(\Lambda/|\epsilon|) \mp i\,|\epsilon|/4v^2$ is the momentum-integrated bare propagator in the retarded/advanced sector, and Λ is a high-energy cutoff [30]. To simplify notation, in what follows we assume that the Fermi level resides in the conduction band $\epsilon > 0$. It is convenient to decompose the self-energy in real and imaginary parts as

$$\mathrm{Re}\,\Sigma = n(\delta\epsilon\,\gamma_0 + m\,\gamma_3), \tag{17}$$

$$-\mathrm{Im}\,\Sigma = n(\eta\,\gamma_0 + \bar\eta\,\gamma_3), \tag{18}$$

with the following definitions: $\delta\epsilon = (\epsilon_+ + \epsilon_-)/2$, $m = (\epsilon_+ - \epsilon_-)/2$, $\eta = (\eta_+ + \eta_-)/2$, and $\bar\eta = (\eta_+ - \eta_-)/2$. Here, $n\,\delta\epsilon$ is a chemical-potential shift that can be reabsorbed in ϵ, while nm is a (small) disorder-induced SOC gap. This result shows that Σ endows quasiparticles with two different lifetimes; we have defined $n\eta$ and $n\bar\eta$ as the respective energy- and spin-gap broadenings. The disorder-averaged propagator reads

$$\mathcal{G}^{R/A}_{\mathbf{k}}(\epsilon) = \frac{(\epsilon \pm i\,n\,\eta)\gamma_0 + n\,(m \mp i\,\bar\eta)\gamma_3 + v\,\gamma^j k_j}{(\epsilon \pm i\,n\,\eta)^2 - n^2(m \mp i\,\bar\eta)^2 - v^2\,k^2}. \tag{19}$$

In order to evaluate the SH conductivity, we also need the form of the charge- and spin-current operators [Eqs. (2) and (3)]. In our model, these are given by $j^z_y = v/2\,\gamma_{13}$ and $v_x = v\,\gamma_1$.

IV. GAUSSIAN DISORDER

A. Anomalous contribution

In this section we consider the weak-scattering regime in the framework of the so-called *Gaussian approximation*. The aim is to show the limitations of this widely used approximation. Consider Eq. (16) for the T matrix; expanding for $|\mathrm{Re}\,g_0 R^2(\alpha_0 \pm \alpha_3)| \ll 1$, one obtains the first two diagrams in Fig. 3. Note that this is different from the naive expansion in the scattering potentials α_0 and α_3 and allows us to treat the two scattering mechanisms on equal footing. Keeping the second (rainbow) diagram is equivalent to considering a random impurity potential with a Gaussian white-noise distribution [40],

$$\langle V(\mathbf{x})\rangle_{\rm dis} = 0, \tag{20}$$

$$\langle V(\mathbf{x})V(\mathbf{x}')\rangle_{\rm dis} = n\,R^4\,M^2\,\delta(\mathbf{x} - \mathbf{x}'). \tag{21}$$

This model has been widely used to study disordered systems. Note that the zero average condition of the random potential comes from the fact that the first diagram in the T-matrix expansion involves only the real part of the self-energy. In standard (parabolic) systems, one can generally readsorb the real part of the self-energy in a redefinition of the Fermi energy; therefore one can always recenter the distribution around zero. In the present case, the real part of the self-energy also contains a random spin-gap term (absent in the clean Hamiltonian), and therefore it cannot be renormalized away. However, at the level of the Gaussian approximation, one can show that adding the random spin-gap term does not modify the leading-order result for the SH conductivity; therefore we will ignore this term henceforth. The imaginary part of the self-energy is given by the Born limit expression

$$\mathrm{Im}\Sigma(\epsilon) = \langle V(\mathbf{x})V(\mathbf{x}')\rangle_d\,\mathrm{Im}G_0(\mathbf{x},\mathbf{x}';\epsilon) \tag{22}$$

$$= n\,R^4\,M^2\frac{\epsilon}{4v^2} = n(\eta\,\gamma_0 + \bar\eta\,\gamma_3), \tag{23}$$

which reproduces the definition of the imaginary part of the self-energy given in Sec. III. However, in the Gaussian model the actual values of the energy broadening parameters are $\eta_\pm \simeq R^4(\alpha_0 \pm \alpha_3)^2\epsilon/(4v^2)$.

In order to study the transport properties of the system, one needs to consider disorder insertions in the four-point function, leading to the vertex corrections. At the level of the Gaussian approximation, impurity scattering contributes to a single ladder diagram (Fig. 4), connecting the advanced and retarded sectors of the response function. The renormalized vertex can be expressed as $\tilde v_x = v_x + \delta v_x$, where v_x is the bare vertex and δv_x are the corrections due to impurity scattering.

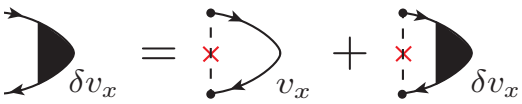

FIG. 4. Bethe-Salpeter equation for the standard vertex correction δv_x. Black dots connected by a dashed line represent impurity potential M insertions, while the red crosses represent an impurity-density insertion.

In order to take into account multiple independent scatterings, one needs to resum the ladder series self-consistently by writing the Bethe-Salpeter equation

$$\delta v_x = \bar{v}_x + n\,R^4 \sum_{\mathbf{k}} M\mathcal{G}^R_{\mathbf{k}}\delta v_x \mathcal{G}^A_{\mathbf{k}} M, \tag{24}$$

where $\bar{v}_x$ contains only the ladder part (see Fig. 4). At leading order in the impurity density we find

$$\bar{v}_x = n\,R^4 \int \frac{d^2k}{(2\pi)^2}\left\{M\mathcal{G}^R_{\mathbf{k}} v_x \mathcal{G}^A_{\mathbf{k}} M\right\} \tag{25}$$

$$= v(a\gamma_1 + b\gamma_{13}), \tag{26}$$

with

$$a \simeq \frac{\left(\alpha_0^2-\alpha_3^2\right)}{2\left(\alpha_0^2+\alpha_3^2\right)}, \quad b \simeq \frac{nR^4}{2v^2}\frac{\alpha_0\alpha_3\left(\alpha_0^2-\alpha_3^2\right)}{\left(\alpha_0^2+\alpha_3^2\right)}. \tag{27}$$

Note that the b coefficient starts at order n, while a is independent of n. The only matrix elements contributing to the vertex renormalization are those proportional to γ_1 and γ_{13}. This means that we can decompose the vertex part in the second diagram of Fig. 4 as $\delta v_x = \delta v_x^1\,\gamma_1 + \delta v_x^2\,\gamma_{13}$. Using this ansatz in the Bethe-Salpeter equation for the vertex part and taking the trace of δv_x together with γ_1 or γ_{13}, we obtain

$$\delta v_1 = \frac{v\left(\alpha_0^2-\alpha_3^2\right)}{\alpha_0^2+3\,\alpha_3^2}, \quad \delta v_2 = 2\,n\,R^4\frac{\alpha_0\,\alpha_3\left(\alpha_0^4-\alpha_3^4\right)}{v\left(\alpha_0^2+3\,\alpha_3^2\right)^2}. \tag{28}$$

In this way, the renormalized vertex can be written as $\tilde{v}_x = (v+\delta v_1)\,\gamma_1 + \delta v_2\,\gamma_{13}$. Using the renormalized vertex into the expression for the SH conductivity and multiplying by a factor of 2 to account for valley degeneracy, we finally obtain the SH conductivity in the noncrossing approximation

$$\sigma^{\rm nc}_{\rm SH}\big|_{\rm Gauss.} = 2\int \frac{d^2k}{(2\pi)^2}\,{\rm Tr}\left[j_y^z\mathcal{G}^R_{\mathbf{k}}(\epsilon)\tilde{v}_x\,\mathcal{G}^A_{\mathbf{k}}(\epsilon)\right] \tag{29}$$

$$= \frac{8e^2}{h}\frac{\alpha_0\alpha_3\left(\alpha_0^2+\alpha_3^2\right)}{\left(\alpha_0^2+3\alpha_3^2\right)^2} \equiv Q^{\rm G}_{\rm nc}. \tag{30}$$

This result suggests an energy-independent SH conductivity. However, as we discussed in Ref. [31], this is an artifact of the Gaussian model. The limitations of the Gaussian approximation and their implications for the correct analysis of the extrinsic SHE will be discussed in Sec. V A. We finalize this section by pointing out the striking similarity between the above result and the noncrossing Hall conductivity for the 2D massive Dirac band with Gaussian scalar disorder [37,45]. The expression for the Hall conductivity σ_{xy} [see, e.g., Eq. (3) in Ref. [37]] can be recovered by multiplying the right-hand side of Eq. (30) by $(-1)\times 1/2$ (the minus sign is to obtain an xy response, and the $1/2$ factor is to remove the valley degeneracy) and sending $\alpha_0 \to \epsilon$ and $\alpha_3 \to m$, where m in the AHE represents the band gap. The straightforward mapping between the two results is not accidental and can be traced back to the similar structure of the dressed propagators in both models [see Eq. (19)].

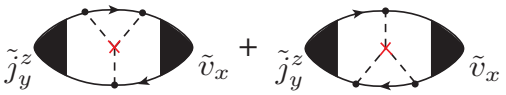

FIG. 5. Y diagrams contributing at order V^3. The dashed lines represent contractions of the impurity potentials, and the red crosses represent an impurity-density insertion.

B. Skew scattering

Within the weak Gaussian approximation it is not possible to assess the effect of skew-scattering events. This is easy to understand by expanding the T matrix: the Gaussian term can only describe the width of the disorder distribution but not its skewness. For this reason, one needs to include order V^3 terms [see also Sec. V B]. In the standard treatments, this is done by allowing for a "non-Gaussian" average of the form

$$\langle V(\mathbf{x})V(\mathbf{x}')V(\mathbf{x}'')\rangle_{\rm dis} = nR^6M^3\delta(\mathbf{x}-\mathbf{x}')\delta(\mathbf{x}'-\mathbf{x}''). \tag{31}$$

It should be noted that in the standard approach, three-point correlators are only used to evaluate the disorder average of the four-point function but not of the self-energy, which is still evaluated at the Gaussian level. Here, we follow this approach and show that it indeed leads to a consistent result in the weak-scattering regime. Using the "non-Gaussian" average prescription of Eq. (31) in the four-point function, one obtains the so-called Y diagrams represented in Fig. 5 (b_2 and b_3 in Fig. 2). In the spirit of the perturbative approach of this section, Y insertions and vertex corrections are treated as if they represent two separate processes. On the other hand, in Ref. [31] we showed that Y insertions are themselves part of the vertex corrections. We will return to this important issue in the following section. Finally, note that in the perturbative approach one also needs to dress the spin vertex $\tilde{j}_y^z = (v+\delta v_1)/2\gamma_{13} + \delta v_2/2\gamma_1$ (see Fig. 5).

It is convenient to recast the expression for the conductivity in terms of proper spin (Γ_y^z) and charge (Γ_x) vertices

$$\sigma_Y = nR^6\,{\rm Tr}\left\{\Gamma_y^z g^R M\Gamma_x + \Gamma_y^z\Gamma_x M g^A\right\}, \tag{32}$$

where

$$\Gamma_y^z = \int \frac{d^2k}{(2\pi)^2} M\mathcal{G}^A_{\mathbf{k}}\,\tilde{j}_y^z\mathcal{G}^R_{\mathbf{k}}M, \tag{33}$$

$$\Gamma_x = \int \frac{d^2k}{(2\pi)^2}\mathcal{G}^R_{\mathbf{k}}\tilde{v}_x\mathcal{G}^A_{\mathbf{k}}, \tag{34}$$

where $g^{R/A}$ are the integrated, dressed Green's functions

$$g^{R/A} \simeq -\frac{(\epsilon \pm \imath n\eta)\gamma_0 + n(m \mp \imath\bar{\eta})\gamma_3}{4\pi v^2} \times \left[\pm\imath\pi + 2\ln\left(\frac{\Lambda}{\epsilon}\right)\right]. \tag{35}$$

At leading order we obtain

$$\Gamma_y^z \simeq \frac{R^4\alpha_0\alpha_3\left(\alpha_0^4-\alpha_3^4\right)}{v\left(\alpha_0^2+3\alpha_3^2\right)^2}\gamma_1 + \frac{v(\alpha_0^2-\alpha_3^2)}{2n\left(\alpha_0^2+3\alpha_3^2\right)}\gamma_{13}, \tag{36}$$

$$\Gamma_x \simeq \frac{v}{nR^4\left(\alpha_0^2+3\alpha_3^2\right)}\gamma_1 + \frac{2\alpha_0\alpha_3\left(\alpha_0^2+\alpha_3^2\right)}{v\left(\alpha_0^2+3\alpha_3^2\right)^2}\gamma_{13}. \tag{37}$$

These are the terms responsible for the semiclassical skew-scattering term in Eq. (1). However, we would like to remark that order $O(n^0)$ terms resulting from Eq. (32) should, in principle, be added to the anomalous contribution coming from the empty bubble. At leading order in the impurity density we find

$$\sigma_Y = \frac{2e^2}{h}\frac{\epsilon\alpha_3\left(\alpha_0^2-\alpha_3^2\right)}{nR^2\left(\alpha_0^2+3\alpha_3^2\right)^2}. \tag{38}$$

In the perturbative approach, the skew-scattering contribution to $\sigma_{\rm SH}$ increases linearly with the energy. In addition, this result predicts that the skew scattering vanishes identically for potentials satisfying $\alpha_0 = \pm\alpha_3$. As shown in the next section, this is an exact symmetry of the model that is preserved at all orders in perturbation theory.

V. BEYOND GAUSSIAN APPROXIMATION

A. Nonperturbative diagrammatic approach

In this section we review the self-consistent treatment of SH response functions introduced by the authors in Ref. [31]. The self-consistent calculation of $\sigma_{\rm SH}$ cures the spurious energy-independent anomalous contribution obtained in the Gaussian approximation and also provides an expression valid for arbitrarily strong scattering potentials. In this approach, one uses the full T matrix both in the self-energy and in the four-point function. The T matrix provides a resummation of all moments of the random disorder distribution in the Markovian (uncorrelated) approximation [40,50]. In general, the distribution of a random variable can be defined by its moments: the "Gaussian" term (or variance) only contains information about the width of the distribution (the deviation from the average), while the third (skewness) and fourth (kurtosis) moments give information about its actual shape [48]. Higher-order moments further define the shape of the distribution. In Sec. IV A, we used the Born criterion to perform a moment expansion up to second order. In its common (and widely used) form, the Born criterion is a statement about the *magnitude* of the scattering potential, and its validity is justified on purely perturbative grounds. This simple criterion has been used to justify the evaluation of the anomalous term (QSJ) by keeping just the second moment. While this argument holds for Hamiltonians with trivial symmetry structure or a single energy scale, it is not generally true otherwise. In our model, for example, by keeping only the Gaussian moment in the T-matrix expansion, the resulting spin current only accounts for symmetric scattering processes. Below, we show that by keeping higher-order moments of the disorder distribution, one can access physically distinguishable processes contributing to the SH current at the same order in α_0 and α_3 as the Gaussian one (QSJ).

As shown in Fig. 2, the expansion of the T matrix in the four-point function [second line of Eq. (11)] corresponds to a series of two-particle noncrossing diagrams containing multiple insertions of the bare scattering potential. The ladder corrections yielding the QSJ contribution and the Y diagrams describing skew scattering in the weak-scattering regime have already been considered in Sec. IV. In order to describe skew scattering and anomalous processes on equal footing, we need to solve for the complete four-point function. Diagrammatically, the latter corresponds to the full series of topologically equivalent two-particle noncrossing diagrams shown in the first two lines of Fig. 2. As explained in Sec. II, this is done by introducing a fully dressed vertex function by exchanging $M \to T^\lambda$ in Eq. (27). We find

$$\bar{v}_x = n\int \frac{d^2k}{(2\pi)^2}\,\hat{T}\mathcal{G}^R_{\mathbf{k}}v_x\mathcal{G}^A_{\mathbf{k}}\hat{T}^* = v(a\gamma_1 + b\gamma_{13}) \tag{39}$$

and

$$a \simeq \epsilon\frac{\eta_+\eta_- + \epsilon_+\epsilon_-}{4v^2(\eta_+ + \eta_-)} - nf_a(\eta_+,\eta_-,\epsilon_+,\epsilon_-), \tag{40}$$

$$b \simeq \epsilon\frac{\eta_+\epsilon_- - \eta_-\epsilon_+}{4v^2(\eta_+ + \eta_-)} + nf_b(\eta_+,\eta_-,\epsilon_+,\epsilon_-), \tag{41}$$

where f_a and f_b are complicated functions of $\eta_\pm,\epsilon_\pm$; explicit expressions are given in Appendix A.

Comparing with the Gaussian expression in Eq. (27), we see a qualitative difference, namely, that the coefficient b now contains a term that is independent of the impurity density n. It is evident that the self-consistent method treats on equal footing the charge and the spin vertices (note the similar structures of a and b coefficients). Indeed, it is easy to see that vertex corrections generate an effective spin-spin $(j_y^z - j_y^z)$ current response function that is ultimately responsible for skew scattering $\mathcal{S}(\epsilon)$. We anticipate here that this additional term in b is also responsible for the nonvanishing of the crossing Ψ diagrams evaluated in Sec. VI.

Solving the Bethe-Salpeter equation for the T-matrix-dressed vertex (see Fig. 6), we see that the additional term in b responsible for skew scattering also influences $\mathcal{Q}$, meaning that skew scattering and QSJ mechanisms are never truly separated. In Ref. [31] we obtained the full SH conductivity in

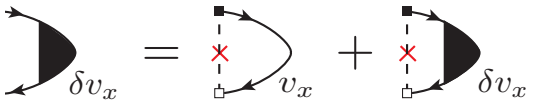

FIG. 6. Bethe-Salpeter equation for the full vertex correction δv_x. Solid (open) squares connected by a dashed line represent T- (T^*-) matrix insertions, while the red crosses represent an impurity-density insertion.

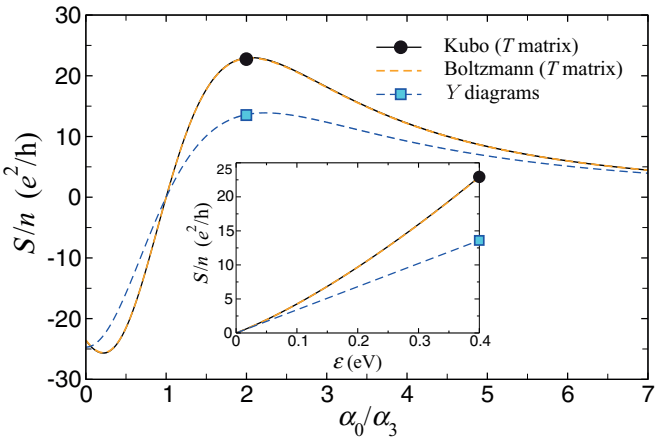

FIG. 7. Semiclassical skew-scattering contribution $\mathcal{S}(\epsilon)/n$. The various approaches are self-consistent LRT, the Y-diagram approximation, and the Boltzmann prediction. The calculation has $R = 6$ nm, $\alpha_3 = 10$ meV, $n = 10^{12}$ cm^{-2}, and $\epsilon = 0.4$ eV. The inset shows the variation with the Fermi energy for $\alpha_0 = 20$ meV.

the noncrossing approximation,

$$\sigma_{\rm SH} = \frac{\epsilon\delta v_{20}}{2nv\eta} + \left\{ \frac{\epsilon\delta v_{22} + 2(v+\delta v_{10})\bar{\eta}}{2v\eta} - \delta v_{20}\left(\frac{1}{\pi v} + \frac{\bar{\eta}m}{2v\eta^2}\right)\right\} \equiv \mathcal{S}(\epsilon)/n + \mathcal{Q}_{\rm nc}(\epsilon), \quad (42)$$

in units of e^2/h. The explicit form of the vertex corrections δv_{ij} is given in Appendix A (for calculation details refer to the Supplemental Material in Ref. [31]).

Discussion

We begin our discussions with the skew-scattering contribution to the SH conductivity, $S(\epsilon)/n$. The improvement over the weak-scattering (Y-diagram) approximation is borne out in Fig. 7, which shows the SH conductivity generated by impurities with a large radius (in our model this is tantamount to a strong-scattering potential). One sees that Y diagrams fail to provide an accurate result, even though the basic trends are still captured. (We expect even stronger discrepancies to arise in models displaying multiple impurity resonances, such as the clustered-adatom/nanoparticle potentials considered in Ref. [14].) We finally note that for our δ-impurity model, the range of validity of the Y-diagram approximation is linked to the strength of the SOC and reads $|{\rm Re}g_0R^2\alpha_3| \ll 1$. When $\alpha_0 = \pm\alpha_3$, the vertex function δv_{20} vanishes identically, and thus $\mathcal{S}(\epsilon) = 0$. This situation corresponds to a potential localized on one of the sublattices, which always leads to symmetric scattering amplitudes (see Sec. V B).

We now discuss the anomalous term, historically associated with QSJ events. Two approaches are normally employed: (i) the standard diagrammatic approach with the empty bubble dressed with ladder diagrams (Sec. IV A) and (ii) the generalized semiclassical transport equations accounting for corrections to the distribution function and velocity operator arising from side-jump accumulation [33]. However, the QSJ is far from being the only mechanism yielding an anomalous contribution. For instance, as noted by Sinitsyn [32], incoherent multiple skew scattering resulting from the dressing of the wave functions with an average SOC also leads to a parametrically equivalent contribution. In the Boltzmann formalism, the latter can be incorporated heuristically by means of a virtual crystal approximation, $H_0 \to H_0 + \Sigma$. The transition rates are then computed with respect to self-energy dressed wave functions, which results in anomalous-type $O(n^0)$ corrections. Within the quantum LRT formalism, the self-energy correction is naturally accounted for in the disordered Green's functions. Since the average SOC is linear in the impurity density, incoherent multiple scattering can usually be safely neglected. In the full noncrossing result [Eq. (42)] this is the term proportional to the spin gap m. There are other mechanisms that can lead to a meaningful contribution, however, of the same order of QSJ or even stronger. As mentioned in the Introduction, quantum coherent multiple scattering (encoded in two-particle crossing diagrams) gives rise to an anomalous contribution. This was recently discovered in a minimal model of the AHE with Gaussian disorder [37]. We will confirm the crucial role played by quantum coherent processes in Sec. VI.

A careful inspection of $\mathcal{Q}_{\rm nc}$ discloses an anomalous contribution that cannot be linked to any of the aforementioned processes: this is one of the central results of this work. In order to establish the origin of this new contribution, it is convenient to compare the full noncrossing expression with the Gaussian result $\mathcal{Q}^{\rm G}_{\rm nc}$ [Eq. (30)]. In addition to a weak Fermi energy dependence absent in the Gaussian approximation, $\mathcal{Q}_{\rm nc}$ contains qualitatively different terms. These terms arise from different physical processes of the same order as the Gaussian ones and therefore cannot be neglected *a priori*. In order to see this explicitly, we consider the weak-scattering limits of $\mathcal{Q}_{\rm nc}$ in the formal $\epsilon \to 0$ limit,

$$\mathcal{Q}_{\rm nc}(\epsilon \to 0) \simeq \begin{cases} 8(\alpha_3/\alpha_0), & \alpha_3 \ll \alpha_0, \\ \frac{40}{27}(\alpha_0/\alpha_3), & \alpha_3 \gg \alpha_0. \end{cases} \quad (43)$$

The above expression deserves a comment. Although the $\epsilon \to 0$ limit can be formally taken in Eq. (42), in this limit $k_F l \to 0$, and the original perturbative series diverges; that is, terms with higher powers of n become increasingly important. Ignoring this technicality, we find that the Gaussian result [Eq. (30)] is only recovered for $\alpha_3 \ll \alpha_0$, whereas in the opposite limit, $\alpha_3 \gg \alpha_0$, the Gaussian approximation yields $Q^{\rm G}_{\rm nc} \simeq 8/9(\alpha_0/\alpha_3)$, which differs from the result in Eq. (43). The former limit corresponds to the case when the SOC term is smaller than any other energy scale in the system. In this case, the parity-symmetry-breaking moments of the disorder distribution give a negligible contribution, and higher moments can be safely neglected. This limit corresponds to the standard Born regime. In the opposite limit, the SOC term becomes the dominant term in the impurity potential, meaning that parity-symmetry-breaking moments *must* be included. The resummation scheme used to obtain Eq. (42) captures this important nonperturbative feature. Indeed, we have checked that higher-order-potential insertions in the vertex corrections are responsible for the different prefactor in Eq. (43). We thus attribute the enhanced anomalous contribution reported here to skew-scattering corrections to QSJ processes.

B. Semiclassical approach: Skew scattering

Semiclassical transport theory provides a simple framework to tackle electronic transport in materials. Broadly speaking, semiclassical approaches are expected to be accurate in the $k_F l \gg 1$ limit, where the use of classical distribution functions $f(\mathbf{x},\mathbf{p},t)$ is justified [49]. The link between Boltzmann transport theory and the quantum diagrammatic approach has been illustrated recently for 2D massive Dirac fermions in the context of the AHE [45]. In that work, a generalization of the standard Boltzmann transport equations (BTEs) informed by an elegant adiabatic semiclassical wave-packet dynamics analysis [32,33] is employed to assess the skew-scattering and side-jump contributions to the conductivity. The results obtained from the generalized BTEs are then matched one to one to particular Kubo-Streda diagrams. It is important to note that the correspondence between the two formalisms in Ref. [45] is established for a simple (scalar) impurity model and limited to the weak-scattering regime. Our findings in the previous section clearly show that weak Gaussian approximations break down due to the intricate correlated nature of QSJ and skew scattering arising from the nontrivial structure of the impurity potential. This suggests that a simple correspondence between the anomalous contribution $\mathcal{Q}(\epsilon)$ obtained from generalized BTEs and the rigorous quantum diagrammatic technique may not exist in general. Nevertheless, one can use Boltzmann theory to evaluate the leading (semiclassical) term in the conductivity expansion (1).

In what follows, we show by explicit calculation that the skew-scattering contribution computed by means of an exact solution of linearized BTEs *quantitatively agrees* with the nonperturbative diagrammatic calculation over a wide range of scattering regimes. The starting point of our semiclassical analysis is the standard BTE for the electronic motion in a uniform system,

$$\frac{\partial n_\sigma}{\partial t} + \dot{\mathbf{k}} \cdot \partial_{\mathbf{k}} n_\sigma = \mathcal{I}[n_\sigma]. \tag{44}$$

In the above, $n_\sigma \equiv n_\sigma(\mathbf{k},t)$ is the distribution function, $\sigma = \pm 1$ ($\uparrow$ and $\downarrow$, respectively) labels the spin projection, $\dot{\mathbf{k}} \equiv d\mathbf{k}/dt$, and $\mathcal{I}[\cdot]$ denotes the collision integral. For a small external perturbation, the linearized BTEs characterizing the steady state for up and down spin species read

$$-\mathcal{E} v_{\mathbf{k},x} \left(\frac{\partial n^0}{\partial \epsilon}\right)_{\epsilon=\epsilon(\mathbf{k})} = \mathcal{I}[n_\sigma(\mathbf{k})], \tag{45}$$

where we used the classical equation of motion $\dot{\mathbf{k}} = -\mathcal{E}\hat{x}$ to simplify the expression, $\mathbf{v}_\mathbf{k}$ denotes the band velocity of pristine graphene, i.e., $v_\mathbf{k} = v(\cos\theta_\mathbf{k}, \sin\theta_\mathbf{k})^{\mathrm{t}}$, and n^0 is the equilibrium Fermi-Dirac distribution function. In our model with spin-conserving impurities, the collision integral does not mix opposite spins, and hence it reduces to its familiar form in paramagnetic systems,

$$\mathcal{I}[n_\sigma(\mathbf{k})] = \sum_{\mathbf{k}'} [n_\sigma(\mathbf{k}') - n_\sigma(\mathbf{k})] W_\sigma(\mathbf{k},\mathbf{k}'), \tag{46}$$

with the quantum-mechanical transition probability given by the generalized Fermi's golden rule

$$W_\sigma(\mathbf{k},\mathbf{k}') = 2\pi n \left|T^\sigma_{\mathbf{k}'\mathbf{k}}\right|^2 \delta(\epsilon_\mathbf{k} - \epsilon_{\mathbf{k}'}), \tag{47}$$

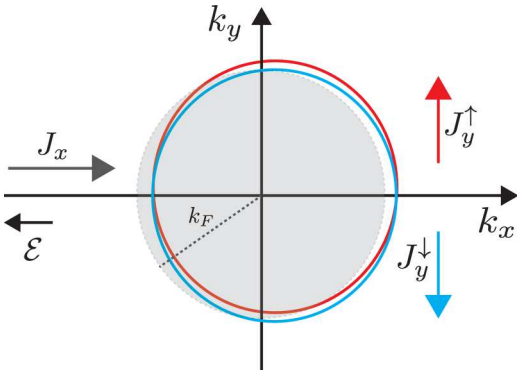

FIG. 8. Illustration of the establishment of a net transverse spin current due to the antisymmetric term in the distribution function Eq. (49).

where $T^\sigma_{\mathbf{k}'\mathbf{k}} = \langle u_{\mathbf{k}'},\sigma|\hat{T}|u_\mathbf{k},\sigma\rangle$ and $|u_\mathbf{k},\sigma\rangle = e^{-i\mathbf{k}\cdot\mathbf{r}}|\psi^0_\mathbf{k}\rangle \otimes |\sigma\rangle$ denotes conduction-band spinors. Using the explicit form of the T matrix for our model [see Eq. (16)] and $|u_{\mathbf{k},\sigma}\rangle = (1, e^{i\theta_\mathbf{k}})^{\mathrm{t}} \otimes |\sigma\rangle$, we easily find

$$T^\sigma_{\mathbf{k}'\mathbf{k}} = \sum_{p=\pm 1} \frac{T_p}{4}[(1+p\sigma) + (1-p\sigma)e^{-i\theta}] \equiv T^\sigma(\theta), \tag{48}$$

where $\theta = \theta_{\mathbf{k}'} - \theta_\mathbf{k}$ is the scattering angle and $T_\pm$ are as given in Eq. (16). From the above expression, it is clear that the scattering-amplitude probabilities possess a right-left asymmetry $|T^\sigma(\theta)| \neq |T^\sigma(-\theta)|$ as long as $T_+ \neq T_-$, which occurs whenever $\alpha_3 \neq 0$ and $\alpha_3 \neq \alpha_0$. The solution of Eq. (45) is given by $n_\sigma(\mathbf{k}) = n^0 + \delta n_\sigma(\mathbf{k})$, where $\delta n_\sigma(\mathbf{k})$ consists of two parts,

$$\delta n_\sigma(\mathbf{k}) = A^\sigma_\parallel \cos\theta_\mathbf{k} + A^\sigma_\perp \sin\theta_\mathbf{k}, \tag{49}$$

a standard longitudinal transport term $A^\sigma_\parallel \propto \tau^\sigma_{xx}$ and a skew-scattering contribution $A^\sigma_\perp \propto \tau^\sigma_{yx}$. The establishment of a net transverse spin current due to the antisymmetric term in the distribution function (49) is illustrated in Fig. 8.

The charge longitudinal and SH conductivities are then obtained according to $\sigma_{xx} = J_x/\mathcal{E}$ and $\sigma^z_{yx} = \mathcal{J}_y/\mathcal{E}$, with

$$J_x = -g_v \int \frac{\Omega d^2k}{(2\pi)^2}[\delta n_\uparrow(\mathbf{k}) + \delta n_\downarrow(\mathbf{k})] v_{\mathbf{k},x}, \tag{50}$$

$$\mathcal{J}_y = -g_v \int \frac{\Omega d^2k}{(2\pi)^2}[\delta n_\uparrow(\mathbf{k}) - \delta n_\downarrow(\mathbf{k})] v_{\mathbf{k},y}, \tag{51}$$

where $g_v = 2$ is the valley degeneracy factor. As shown in Ref. [14], the zero-temperature conductivities admit an exact closed form,

$$\begin{aligned} \sigma_{xx} &= 2\epsilon\tau_{xx}, \quad \tau_{xx} \equiv \frac{\tau^\uparrow_\parallel}{1+(\frac{\tau^\uparrow_\parallel}{\tau^\uparrow_\perp})^2}, \\ \sigma_{\mathrm{SH}} &= 2\epsilon\tau^z_{yx}, \quad \tau^z_{yx} \equiv \frac{\tau^\uparrow_\perp}{1+(\frac{\tau^\uparrow_\perp}{\tau^\uparrow_\parallel})^2}, \end{aligned} \tag{52}$$

in terms of transport and skew-scattering relaxation times, defined by

$$\frac{1}{\tau_{\parallel}^{\sigma}} = \frac{n\epsilon}{2\pi v^2}\int d\theta(1-\cos\theta)|T^{\sigma}(\theta)|^2, \tag{53}$$

$$\frac{1}{\tau_{\perp}^{\sigma}} = \frac{n\epsilon}{2\pi v^2}\int d\theta\sin\theta|T^{\sigma}(\theta)|^2, \tag{54}$$

respectively [14]. Combining Eq. (48) and Eqs. (53) and (54), we find after straightforward calculations

$$\frac{1}{\tau_{\parallel}^{\sigma}} = \frac{n\epsilon}{4v^2}(\epsilon_+^2+\epsilon_-^2+\eta_+^2+\eta_-^2-\eta_+\eta_--\epsilon_+\epsilon_-), \tag{55}$$

$$\frac{1}{\tau_{\perp}^{\sigma}} = \frac{n\epsilon\sigma}{8v^2}(\epsilon_-\eta_+-\epsilon_+\eta_-). \tag{56}$$

Inserting the above expressions in Eq. (52), we arrive at the desired result:

$$\sigma_{\rm SH} = \frac{16e^2}{h}\left(\frac{v^2}{n}\right)\frac{\epsilon_-\eta_+-\epsilon_+\eta_-}{(\epsilon_-\eta_+-\epsilon_+\eta_-)^2+4(\epsilon_+^2+\epsilon_-^2+\eta_+^2+\eta_-^2-\eta_+\eta_--\epsilon_+\epsilon_-)^2}. \tag{57}$$

In Fig. 7 we compare the skew-scattering contribution evaluated with Eq. (57) with the self-consistent diagrammatic LRT expression [Eq. (42)]. We focus on the strong-scattering regime, $|{\rm Re}g_0R^2\alpha_3|\gtrsim 1$, where the Y-diagram approximation breaks down (Sec. V A). The two results are virtually indistinguishable. To better understand this, we performed an expansion in $|{\rm Re}g_0R^2(\alpha_0\pm\alpha_3)|\ll 1$ and found that the two expressions agree up to the third order. At higher orders the expressions no longer coincide but are numerically very similar. The different mathematical structures of $\mathcal{S}(\epsilon)$ in the two approaches can be rationalized as follows. In the standard Boltzmann description, electrons feel the scattering potential only when they scatter off an impurity. Between two successive scatterings, the electrons follow a straight trajectory determined by the classical equation of motion [50]. Mathematically, this is expressed by the fact that the matrix elements in Eq. (47) are evaluated with the eigenstates of the clean system. On the other hand, in the Kubo formula disorder enters in two places, the self-energy and the vertex parts (see Sec. II). The latter gives the transport relaxation time, while the former corresponds to dressing the bare eigenstates with disorder. We would like to mention that the above picture is extremely clear when using the functional approach [48]. There, the self-energy is obtained from the mean-field solution (average disorder field seen by the electron), and the vertex part is obtained by considering fluctuations around this solution, i.e., fluctuations due to local scattering off an impurity. Physically, this means that quantum mechanically the electron's trajectory between successive scattering events is not a straight line but is affected by the background disorder field [50]. As explained in detail in Sec. V A, this is also the reason why the BTE does not capture per se the $\mathcal{Q}_{\rm nc}(\epsilon)$ term, as this is due to the cooperation of self-energy and local scattering effects.

VI. BEYOND THE NONCROSSING APPROXIMATION

Crossing diagrams are usually associated with quantum interference effects and appear with an extra factor of smallness proportional to $(k_Fl)^{-1}$. Indeed, maximally crossed diagrams are responsible for weak localization corrections [40,49]. Recently, Ado *et al.* [37] showed, in the context of the AHE with massive Dirac fermions, that a specific subclass of crossing diagrams also contributes to order $(k_Fl)^0$ to the transverse conductivity. These diagrams (see Fig. 9), appearing at fourth order in the impurity potential insertion, represent rare events in which an electron skew scatters coherently off two impurities located at a distance of the order of the Fermi wavelength $k_F|\mathbf{x}-\mathbf{x}'|\lesssim 1$. Being in the dilute regime, this is a rare event that nevertheless gives rise to an anomalous contribution to the SH conductivity. As often happens in stochastic processes, rare events are associated with big fluctuations above the average and therefore can deeply affect the value of observables. In this section, we evaluate the contribution of the crossing diagrams to the SH conductivity shown in the third line of Fig. 2, first in the context of the Gaussian approximation and then using the full T-matrix formalism.

A. Gaussian model

1. X diagram

The X diagram is obtained by dressing the four-point function with four impurity potentials and two impurity-density terms connecting the retarded and advanced sectors (see Fig. 9). Formally, one needs to take the disorder average

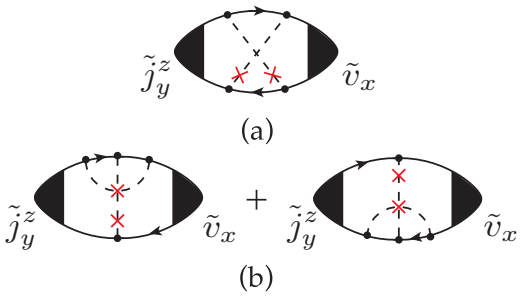

FIG. 9. Diagrams with crossing impurities. (a) X and (b) Ψ diagrams contributing to the SH conductivity. Here $\tilde{j}_y^z$ and $\tilde{v}_x$ are, respectively, the renormalized charge and spin vertices. The dashed lines represent contractions of the impurity potentials, and the red crosses represent an n insertion.

of

$$\sigma_X^{\mathrm{G}} = 2\int\prod_{n=0}^{4}\frac{d^2p_n}{(2\pi)^2}\mathrm{Tr}\{\tilde{j}_y^z\mathcal{G}_{\mathbf{p}}^R\langle V(\mathbf{p}-\mathbf{p_1})\mathcal{G}_{\mathbf{p_1}}^R V(\mathbf{p_1}-\mathbf{p_2}) \times \mathcal{G}_{\mathbf{p_2}}^R\tilde{v}_x\mathcal{G}_{\mathbf{p_2}}^A V(\mathbf{p_2}-\mathbf{p_3})\mathcal{G}_{\mathbf{p_3}}^A V(\mathbf{p_3}-\mathbf{p_4})\rangle_{\mathrm{dis}}\mathcal{G}_{\mathbf{p_4}}^A\}, \quad (58)$$

where $\mathbf{p}_0 \equiv \mathbf{p}$. The X diagram is obtained from the contraction

$$\langle V(\mathbf{p}-\mathbf{p_1})V(\mathbf{p_1}-\mathbf{p_2})V(\mathbf{p_2}-\mathbf{p_3})V(\mathbf{p_3}-\mathbf{p_4})\rangle_{\mathrm{dis}} = \langle V(\mathbf{p}-\mathbf{p_1})V(\mathbf{p_2}-\mathbf{p_3})\rangle_{\mathrm{dis}}\langle V(\mathbf{p_1}-\mathbf{p_2})V(\mathbf{p_3}-\mathbf{p_4})\rangle_{\mathrm{dis}}. \quad (59)$$

In this way we obtain

$$\sigma_X^{\mathrm{G}} = 2(nR^4)^2\int\prod_{n=0}^{2}\frac{d^2p_n}{(2\pi)^2}\mathrm{Tr}\{\left(M\mathcal{G}_{\mathbf{p}}^A\tilde{j}_y^z\mathcal{G}_{\mathbf{p}}^R M\right) \times \mathcal{G}_{\mathbf{p_1}}^R\left(M\mathcal{G}_{\mathbf{p_2}}^R\tilde{v}_x\mathcal{G}_{\mathbf{p_2}}^A M\right)\mathcal{G}_{\mathbf{Q}-\mathbf{p_1}}^A\}, \quad (60)$$

where $\mathbf{Q} = \mathbf{p} + \mathbf{p}_2$ and the terms in parentheses constitute the proper vertices. Due to the presence of $\mathbf{Q}$, the momentum integrals do not factorize. Generally, the nonfactorization of the integrals encodes correlation physics. In this case, it describes an event in which the probability of an electron scattering off a second nearby impurity depends on the scattering probability at the first impurity. In order to evaluate this contribution, we follow the approach of Ref. [37] and rewrite σ_X^{G} in real space as

$$\sigma_X^{\mathrm{G}} = 2(nR^4)^2\int_{\mathbf{r}}\mathrm{Tr}\{\Gamma_y^z(\mathbf{r})\mathcal{G}^R(-\mathbf{r})\Gamma_x(\mathbf{r})\mathcal{G}^A(-\mathbf{r})\}, \quad (61)$$

with

$$\Gamma_{y,\mathbf{r}}^z = \int\frac{d^2p}{(2\pi)^2}\left(M\mathcal{G}_{\mathbf{p}}^A\tilde{j}_y^z\mathcal{G}_{\mathbf{p}}^R M\right)e^{i\mathbf{p}\cdot\mathbf{r}}, \quad (62)$$

$$\Gamma_{x,\mathbf{r}} = \int\frac{d^2p}{(2\pi)^2}\left(M\mathcal{G}_{\mathbf{p}}^R\tilde{v}_x\mathcal{G}_{\mathbf{p}}^A M\right)e^{i\mathbf{p}\cdot\mathbf{r}}, \quad (63)$$

where $\Gamma_{y,\mathbf{r}}^z$ and $\Gamma_{x,\mathbf{r}}$ are, respectively, the Fourier transforms of the proper spin and charge vertices. We look for contributions of the same order of SH conductivity evaluated in Eq. (29). Since the X conductivity comes with a prefactor of n^2, this means that we need an additional $1/n^2$ factor coming from the integrand. It is therefore enough to keep the part of the renormalized vertex $\tilde{v}_x$ ($\tilde{j}_y^z$) that is independent of n. According to Eq. (28), we take $\tilde{v}_x = F\gamma_1$ and $\tilde{j}_y^z = F/2\gamma_{13}$, where $F = v + \delta v_1$. In order to evaluate the Fourier transform of the proper vertices, we use the relation between the Dirac and Klein-Gordon propagators to write

$$\mathcal{G}_{\mathbf{p}}^{R/A} = \{(\epsilon \pm in\eta)\gamma_0 + n(m \mp i\bar{\eta})\gamma_3 - iv\gamma^j\partial_j\} \times \frac{1}{(\epsilon \pm in\eta)^2 - n^2(m \mp i\bar{\eta})^2 - v^2p^2}, \quad (64)$$

which should be understood in the operator sense. To lowest order in n, the Fourier transform of the proper vertices reads

$$\Gamma_{x,\mathbf{r}} = \frac{F}{n}\sum_{n=0}^{3}a_n(\mathbf{r})\gamma_n, \quad (65)$$

$$\Gamma_{y,\mathbf{r}}^z = \frac{F}{2n}\{b_0(\mathbf{r})\gamma_{54} + b_1(\mathbf{r})\gamma_{23} + b_2(\mathbf{r})\gamma_{31} + b_3(\mathbf{r})\gamma_{12}\}, \quad (66)$$

where the space-dependent coefficients $\{a_n, b_n\}$ are defined in Appendix C. Since the proper vertices already contain a factor of $1/n$, the conductivity can be evaluated using the bare Green's functions instead of the dressed ones [37]. The real-space form of the bare propagator reads

$$\mathcal{G}_0^{R/A}(\mathbf{r}) = \frac{\epsilon\gamma_0 - iv\gamma^j\partial_j}{4v^2}\left[Y_0\left(\frac{\epsilon r}{v}\right) \mp iJ_0\left(\frac{\epsilon r}{v}\right)\right], \quad (67)$$

where J_0 and Y_0 are, respectively, Bessel functions of the first and second kinds (see Appendix B). Using Eqs. (65)–(67) in the expression for the conductivity, Eq. (61), one finally obtains

$$\sigma_X^{\mathrm{G}} = -\frac{8e^2}{h}\frac{\alpha_0\alpha_3\left(\alpha_0^2 - \alpha_3^2\right)}{\left(\alpha_0^2 + 3\alpha_3^2\right)^2}. \quad (68)$$

The X-diagram contribution to the SH conductivity has the basic symmetry of the semiclassical skew scattering; namely, it vanishes when $|\alpha_0| = |\alpha_3|$ [see Eq. (38)].

2. Ψ diagrams

We now evaluate the two Ψ diagrams in Fig. 9(b). The evaluation closely follows that of the X diagram; therefore we only highlight the main steps. For the first diagram, we find in momentum space

$$\sigma_{\Psi,\mathrm{I}}^{\mathrm{G}} = 2(nR^4)^2\int\prod_{n=0}^{2}\frac{d^2p_n}{(2\pi)^2}\mathrm{Tr}\{\left(M\mathcal{G}_{\mathbf{p}}^A\tilde{j}_y^z\mathcal{G}_{\mathbf{p}}^R M\right) \times \mathcal{G}_{\mathbf{k}+\mathbf{p_1}}^R M\mathcal{G}_{\mathbf{p_1}}^R M\left(\mathcal{G}_{\mathbf{p_2}}^R\tilde{v}_x\mathcal{G}_{\mathbf{p_2}}^A\right)\}, \quad (69)$$

where $\mathbf{k} = \mathbf{p} - \mathbf{p}_2$ and, as before, $\mathbf{p}_0 \equiv \mathbf{p}$. The second diagram can be obtained from the first by taking the conjugate of $\sigma_{\Psi,\mathrm{I}}^{\mathrm{G}}$. Also, in this case, it is convenient to move to real space. The Ψ-diagram contribution to the conductivity then reads

$$\sigma_{\Psi}^{\mathrm{G}} = 2(nR^4)^2\int_{\mathbf{r}}\mathrm{Tr}\{\Gamma_y^z(\mathbf{r})\mathcal{G}^R(-\mathbf{r})M\mathcal{G}^R(\mathbf{r})M\chi_x(-\mathbf{r}) + \Gamma_y^z(\mathbf{r})\chi_x(-\mathbf{r})M\mathcal{G}^A(\mathbf{r})M\mathcal{G}^A(-\mathbf{r})\}, \quad (70)$$

where

$$\chi_x(\mathbf{r}) = \int\frac{d^2p}{(2\pi)^2}\left(\mathcal{G}_{\mathbf{p_2}}^R\tilde{v}_x\mathcal{G}_{\mathbf{p_2}}^A\right)e^{i\mathbf{p}\cdot\mathbf{r}} \quad (71)$$

and $\Gamma_{y,\mathbf{r}}^z$ is the same as in Eq. (66). To lowest order in n, the evaluation of the Fourier transform of the proper charge vertex yields

$$\chi_x(\mathbf{r}) = \frac{F}{n}\sum_{n=0}^{2}c_n(\mathbf{r})\gamma_n, \quad (72)$$

where the explicit expressions for the coefficients are given in Appendix C. Performing the real-space integral, we find

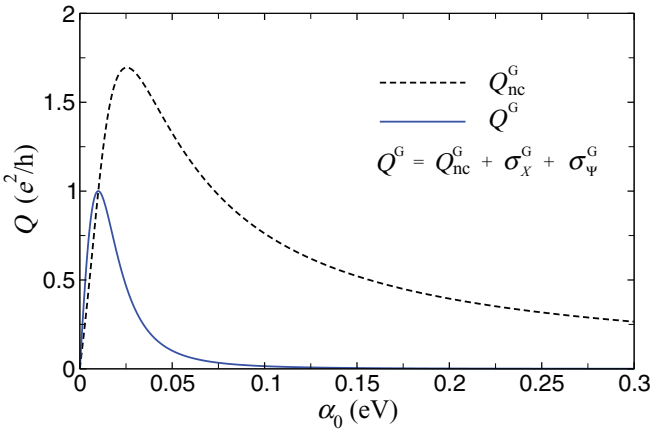

FIG. 10. Total anomalous contribution to the SH conductivity in the Gaussian approximation. The noncrossing result is shown for comparison. The calculation has $\alpha_3 = 10$ meV.

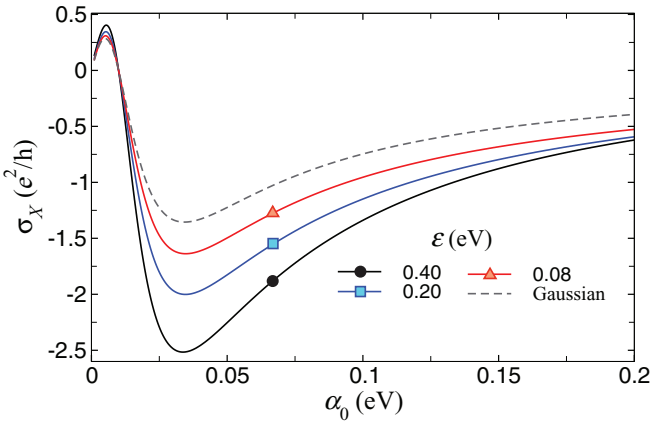

FIG. 11. X conductivity in the full T-matrix approach. The X conductivity is plotted as a function of the scalar disorder potential α_0 for different values of the Fermi energy. As a comparison, we also plot the Gaussian value, formally recovered in the $\epsilon \to 0$ limit. Note that σ_X goes to zero at higher values of α_0, in agreement with the unitary-limit result. The other parameters used in the plot are $\alpha_3 = 10$ meV and $R = 4$ nm.

$\sigma_\Psi = 0$. A similar result was found by Ado *et al.* [37] in the context of the AHE, where the authors also stressed that the vanishing of σ_Ψ is due to the minimal form of the model. One could argue that this is the case also in our model. However, as we show below, we find that the vanishing of σ_Ψ is again an artifact of the Gaussian approximation.

Summing the noncrossing Ψ and X contributions, we finally arrive at

$$\sigma^{\rm G}_{\rm SH} = Q^{\rm G}_{\rm nc} + \sigma^{\rm G}_X + \sigma^{\rm G}_\Psi = \frac{16e^2}{h}\frac{\alpha_0\alpha_3^3}{\left(\alpha_0^2+3\alpha_3^2\right)^2}. \tag{73}$$

The total SH conductivity in the Gaussian approximation is plotted in Fig. 10 as a function of α_0. We see that the crossing diagrams drastically reduce the value of the SH conductivity with respect to the noncrossing approximation.

B. T-matrix evaluation

As we have explained before, the lack of an energy dependence in the expression for the SH conductivity is an artifact of the Gaussian approximation. In Ref. [31] we showed that using the full T matrix, one obtains indeed a Fermi energy dependence of the quantum anomalous SH conductivity $\mathcal{Q}$. Obtaining the correct expression for the energy dependence is crucial for assessing the crossover between semiclassical to quantum anomalous spin transport.

Two main differences arise when performing the calculation of crossing diagrams within the T-matrix approach. First, the b coefficient of the renormalized vertex in Eq. (27) now contains an extra term that is independent of n [see Eq. (39)]. As we showed in Sec. V A, in the noncrossing approximation this additional vertex part is responsible for the semiclassical skew-scattering contribution, introducing an effective spin-spin interaction [31]. Mathematically, the additional vertex part modifies the structure of the proper vertices in Eqs. (65) and (66). For each vertex, we now have two contributions, namely, $\Gamma_{x,\mathbf{r}} = \Gamma^1_{x,\mathbf{r}} + \Gamma^2_{x,\mathbf{r}}$, where

$$\Gamma^1_{x,\mathbf{r}} = \frac{1}{n}\sum_{n=0}^{3}\bar{a}_n(\mathbf{r})\gamma_n, \tag{74}$$

$$\Gamma^2_{x,\mathbf{r}} = \frac{1}{n}\{\bar{b}_0(\mathbf{r})\gamma_{54} + \bar{b}_1(\mathbf{r})\gamma_{23} + \bar{b}_2(\mathbf{r})\gamma_{31} + \bar{b}_3(\mathbf{r})\gamma_{12}\}, \tag{75}$$

and $\Gamma^z_{y,\mathbf{r}} = \Gamma^{z,1}_{y,\mathbf{r}} + \Gamma^{z,2}_{y,\mathbf{r}}$, where now the coefficients are interchanged with respect to the charge vertex, i.e.,

$$\Gamma^{z,1}_{y,\mathbf{r}} = \frac{1}{n}\sum_{n=0}^{3}\bar{b}_n(\mathbf{r})\gamma_n, \tag{76}$$

$$\Gamma^{z,2}_{y,\mathbf{r}} = \frac{1}{n}\{\bar{a}_0(\mathbf{r})\gamma_{54} + \bar{a}_1(\mathbf{r})\gamma_{23} + \bar{a}_2(\mathbf{r})\gamma_{31} + \bar{a}_3(\mathbf{r})\gamma_{12}\}. \tag{77}$$

Second, the single-potential insertions in the crossing bubbles of Fig. 9 need to be replaced with the T matrix, just like we did in Ref. [31] for the ladder diagram. This last step ensures the resummation of all topologically equivalent diagrams. Apart from these differences, the evaluation of the crossing contribution follows the steps in Sec. V A. After a lengthy calculation we obtain the Fermi energy dependence of the X diagram. This is shown in Fig. 11, where we also plot the Gaussian result, Eq. (68), as a guide. The magnitude of the X-diagram contribution increases with Fermi energy, as expected for a skew-scattering contribution. We note that the Gaussian result is recovered from the self-consistent one in the formal $\epsilon \to 0$ limit.

Most importantly, we find that the Ψ diagrams give a *finite* contribution away from the Dirac point. This is shown in Fig. 12, where the Ψ contribution to the SH conductivity is plotted for different values of the Fermi energy. Strikingly, the Ψ diagram is found to result in the dominant contribution to $\mathcal{Q}$ over a wide range of parameters, whereas in the Gaussian approximation this term plays no role. The enhanced quantum coherent contribution away from the Dirac point is one of

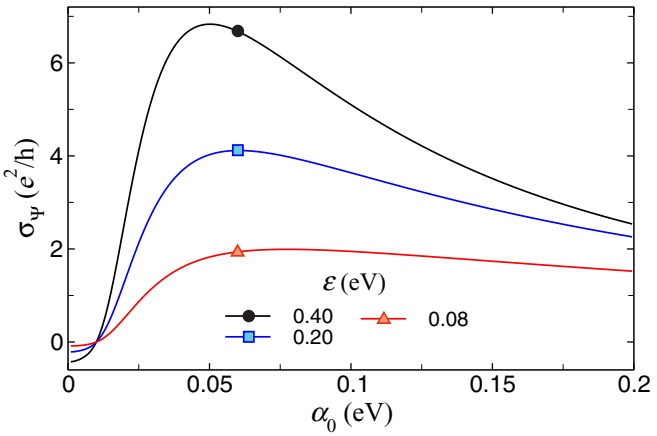

FIG. 12. Ψ conductivity in the full T-matrix approach. The Ψ conductivity is plotted as a function of the scalar potential strength α_0 for different values of the Fermi energy. Note that $\sigma_\Psi \to 0$ as $\epsilon \to 0$. At higher values of α_0, σ_Ψ also goes to zero, in agreement with the unitary-limit result. The other values used in the plot are $\alpha_3 = 0.01$ eV and $R = 4$ nm.

the central findings of the current work. Comparing the Ψ contribution with the semiclassical skew scattering, it is easy to recognize several similarities: σ_Ψ increases as the Fermi energy is increased; independently of the value of ϵ, σ_Ψ is zero if $|\alpha_0| = |\alpha_3|$, and finally, the sign of σ_Ψ depends on the relative magnitude of the scattering terms (an example is shown in Fig. 12, where σ_Ψ becomes negative when $\alpha_0 < \alpha_3$). This term is dominant at high Fermi energy, and therefore it can compete with the semiclassical skew-scattering term, favoring in this way the crossover to the quantum anomalous-dominated SH regime recently discovered in Ref. [31].

VII. CONCLUSIONS

In this work we have presented a detailed analysis of the spin Hall effect in systems of 2D massless Dirac fermions subject to extrinsic spin-orbit interactions with origins in short-range impurities. We have shown that for meaningful scattering potential models, characterized by multiple terms in the low-energy theory or ones generally in the strong scattering regime, the often used Gaussian-type approximations fail to give the correct answers, especially by predicting a spin Hall response function independent of the Fermi energy. In order to overcome these limitations, we introduced a self-consistent quantum diagrammatic approach, in which self-energy operators and vertex corrections in the Kubo-Streda formula are evaluated at the T-matrix level. The extended diagrammatic technique allows us to treat skew scattering and anomalous contributions on equal footing and at all orders in the potential strength by resumming all moments of the disorder distribution. In the noncrossing approximation, we find that the spin Hall conductivity $\sigma_{\rm SH}$ depends on the Fermi energy in a sensible way. The (semiclassical) skew-scattering contribution $\sigma_{\rm SH} \propto n^{-1}$ is shown to quantitatively agree with Boltzmann theory over a wide range of parameters, showing the equivalence between the semiclassical and the quantum linear-response approaches in the presence of spin-orbit interactions and strong impurity scattering. Furthermore, by treating skew scattering and quantum side jumps on equal footing, we find that these two processes are generally correlated as a result of the nontrivial sublattice structure of spin-orbit-active impurities in graphene. This suggests that previous treatments, assuming independent contributions from skew scattering and quantum side-jump events, are not generally valid. Finally, we have evaluated the contribution of an important subclass of crossing diagrams encoding quantum interference corrections and showed they contribute to the anomalous component of the spin Hall conductivity. We have shown that also in this case the Gaussian approximation fails to give the correct picture, especially by predicting the vanishing of a subclass of crossing diagrams. Within the extended T-matrix formalism we not only show that this class of diagrams is nonvanishing but that it dominates the spin Hall conductivity in experimentally relevant parameter regions. Most importantly, these quantum coherent corrections seem to favor the crossover to the anomalous regime recently discussed by the authors in Ref. [31], opening the exciting prospect of detecting signatures of quantum coherent spin Hall phenomena in nonlocal transport experiments. In this work we have focused on impurities leading to local spin-orbit coupling of the intrinsic type, which preserve the point symmetry group D_{6h} of pristine graphene, as well as the out-of-plane spin projection. This has enabled us to obtain exact and simple analytical expressions for some important classes of Kubo-Streda diagrams. In future work, it would be interesting to extend the use of the self-consistent quantum diagrammatic approach discussed here to more realistic impurity potentials in graphene, including both Rashba-like spin-orbit-coupling terms breaking the mirror symmetry about the plane and intervalley terms relevant for atomically sharp impurity potentials [17]. We note that the rigorous quantum diagrammatic technique introduced in this work can be employed to compute generic response functions for disordered spin-orbit coupled electrons, which are relevant for a number of topics from the anomalous Hall effect in ferromagnets to the valley Hall effect in layered materials.

ACKNOWLEDGMENTS

M.M. thanks R. Raimondi and G. Vignale for stimulating discussions. M.M. acknowledges support from the Singapore National Research Foundation under its fellowship program (NRF Award No. NRF-NRFF2012-01). A.F. gratefully acknowledges the financial support of the Royal Society (U.K.) through a Royal Society University Research Fellowship.

APPENDIX A: FUNCTIONS APPEARING IN THE SELF-CONSISTENT APPROACH

$$f_a(\eta_+,\eta_-,\epsilon_+,\epsilon_-) = \frac{(\eta_+ + \eta_-)(\epsilon_+\epsilon_- + \eta_+\eta_-) - \pi(\eta_+ - \eta_-)(\epsilon_+\eta_- - \eta_+\epsilon_-)}{4\pi v^2(\eta_+ + \eta_-)}. \tag{A1}$$

$$f_b(\eta_+,\eta_-,\epsilon_+,\epsilon_-) = \frac{(\eta_+ + \eta_-)(\epsilon_+\eta_- - \eta_+\epsilon_-) + \pi(\eta_+ - \eta_-)(\epsilon_+\epsilon_- + \eta_+\eta_-)}{4\pi v^2(\eta_+ + \eta_-)}. \tag{A2}$$

$$\begin{aligned}\delta v_{10} &= v\frac{4v^2\epsilon(\eta_+ + \eta_-)(\epsilon_+\epsilon_- + \eta_+\eta_-) - \epsilon^2(\eta_+^2 + \epsilon_+^2)(\eta_-^2 + \epsilon_-^2)}{\epsilon^2(\eta_+^2 + \epsilon_+^2)(\eta_-^2 + \epsilon_-^2) - 8\epsilon v^2(\eta_+ + \eta_-)(\epsilon_+\epsilon_- + \eta_+\eta_-) + 16v^4(\eta_+ + \eta_-)^2}.\\ \delta v_{20} &= v\frac{4\epsilon v^2(\eta_+ + \eta_-)(\epsilon_-\eta_+ - \epsilon_+\eta_-)}{\epsilon^2(\eta_+^2 + \epsilon_+^2)(\eta_-^2 + \epsilon_-^2) - 8\epsilon v^2(\eta_+ + \eta_-)(\epsilon_+\epsilon_- + \eta_+\eta_-) + 16v^4(\eta_+ + \eta_-)^2}.\end{aligned} \tag{A3}$$

$$\begin{aligned}\delta v_{11} = \frac{v}{\pi}4v^2(\eta_+ + \eta_-)\{&16v^4(\eta_+ - \eta_-)^2[\pi(\eta_+ + \eta_-)(\eta_+\epsilon_- - \eta_-\epsilon_+) + (\eta_+ + \eta_-)(\eta_+\eta_- + \epsilon_+\epsilon_-)]\\ &- 8\epsilon\pi v^2(\eta_+ + \eta_-)^2(\eta_+^2 + \epsilon_+^2)(\eta_-^2 + \epsilon_-^2) + \epsilon^2(\eta_+^2 + \epsilon_+^2)(\eta_-^2 + \epsilon_-^2)[(\eta_+ + \eta_-)(\eta_+\eta_- + \epsilon_+\epsilon_-)\\ &- \pi(\eta_+ + \eta_-)(\eta_+\epsilon_- - \eta_-\epsilon_+)]\}/[\epsilon^2(\eta_+^2 + \epsilon_+^2)(\eta_-^2 + \epsilon_-^2) - 8\epsilon v^2(\eta_+ + \eta_-)(\epsilon_+\epsilon_- + \eta_+\eta_-) + 16v^4(\eta_+ + \eta_-)^2]^2.\end{aligned} \tag{A4}$$

$$\begin{aligned}\delta v_{22} = \frac{v}{\pi}4v^2(\eta_+ + \eta_-)\{&16v^4(\eta_+ - \eta_-)^2[\pi(\eta_+ - \eta_-)(\eta_+\eta_- + \epsilon_+\epsilon_-) + (\eta_+^2 + \eta_-^2)(\eta_+\epsilon_- - \eta_-\epsilon_+)]\\ &- 8\epsilon\pi v^2(\eta_+ - \eta_-)(\eta_+^2 + \epsilon_+^2)(\eta_-^2 + \epsilon_-^2) + \epsilon^2(\eta_+^2 + \epsilon_+^2)(\eta_-^2 + \epsilon_-^2)[(\eta_+ + \eta_-)(\eta_+\epsilon_- - \eta_-\epsilon_+)\\ &+ \pi(\eta_+ - \eta_-)(\eta_+\eta_- + \epsilon_+\epsilon_-)]\}/[\epsilon^2(\eta_+^2 + \epsilon_+^2)(\eta_-^2 + \epsilon_-^2) - 8\epsilon v^2(\eta_+ + \eta_-)(\epsilon_+\epsilon_- + \eta_+\eta_-) + 16v^4(\eta_+ + \eta_-)^2]^2.\end{aligned} \tag{A5}$$

APPENDIX B: REAL-SPACE FORM OF THE PROPAGATOR

In order to obtain the real space form of the bare propagator, one starts from the operator relation

$$\mathcal{G}_0^{R/A}(\mathbf{r}) = (\epsilon\gamma_0 - iv\gamma^i\partial_i)\mathcal{F}\left(\frac{1}{\epsilon^2 - v^2k^2 \pm i0^+}\right), \tag{B1}$$

where $\mathcal{F}[\cdot]$ stands for Fourier transform. Explicitly,

$$\mathcal{F}\left(\frac{1}{\epsilon^2 - v^2k^2 \pm i0^+}\right) = -\frac{1}{2\pi v^2}K_0\left(\mp i\frac{\epsilon r}{v}\right) = \frac{1}{4v^2}\left[Y_0\left(\frac{\epsilon r}{v}\right) \mp iJ_0\left(\frac{\epsilon r}{v}\right)\right], \tag{B2}$$

where $r \equiv |\mathbf{r}|$. In the last step we have separated the real and imaginary parts of the modified Bessel function $K_0(z)$ using the identity

$$-\frac{2}{\pi}K_\nu(z)e^{-i\pi\nu/2} = Y_\nu(\imath z) - iJ_\nu(iz), \tag{B3}$$

where J_ν and Y_ν are Bessel functions of the first and second kinds, respectively (see, e.g., [51]). The real-space propagator then reads

$$\mathcal{G}_0^{R/A}(\mathbf{r}) = \frac{\epsilon}{4v^2}\left\{\gamma_0\left[Y_0\left(\frac{\epsilon r}{v}\right) \mp iJ_0\left(\frac{\epsilon r}{v}\right)\right] + i(\gamma_1\hat{x}_1 + \gamma_2\hat{x}_2)\left[Y_1\left(\frac{\epsilon r}{v}\right) \mp iJ_1\left(\frac{\epsilon r}{v}\right)\right]\right\}, \tag{B4}$$

where $\hat{x}_i$ is the unit vector in two dimensions.

APPENDIX C: COEFFICIENTS APPEARING IN THE PROPER VERTICES I: GAUSSIAN

Here, we list the coefficients appearing in the definition of the proper vertices. J_ν are Bessel functions of the first kind.

$$a_0(\mathbf{r}) = \frac{i\cos(\theta)J_1\left(\frac{\epsilon r}{v}\right)}{R^4}. \tag{C1}$$

$$a_1(\mathbf{r}) = \frac{(\alpha_0^2 - \alpha_3^2)}{2R^4(\alpha_0^2 + \alpha_3^2)}\left\{J_0\left(\frac{\epsilon r}{v}\right) + \cos(2\theta)\frac{\left[\epsilon r J_0\left(\frac{\epsilon r}{v}\right) - 2vJ_1\left(\frac{\epsilon r}{v}\right) - \epsilon r J_2\left(\frac{\epsilon r}{v}\right)\right]}{2\epsilon r}\right\}. \tag{C2}$$

$$a_2(\mathbf{r}) = \frac{-(\alpha_0^2 - \alpha_3^2)\sin(2\theta)}{R^4(\alpha_0^2 + \alpha_3^2)\epsilon}\left\{\frac{\epsilon r J_0\left(\frac{\epsilon r}{v}\right) - 2vJ_1\left(\frac{\epsilon r}{v}\right) - \epsilon r J_2\left(\frac{\epsilon r}{v}\right)}{4r}\right\}. \tag{C3}$$

$$a_3(\mathbf{r}) = \frac{2i\alpha_0\alpha_3\cos(\theta)J_1\left(\frac{\epsilon r}{v}\right)}{R^4(\alpha_0^2 + \alpha_3^2)}. \tag{C4}$$

$$b_0(\mathbf{r}) = \frac{i\sin(\theta)J_1\left(\frac{\epsilon r}{v}\right)}{R^4}. \tag{C5}$$

$$b_1(\mathbf{r}) = \frac{-\left(\alpha_0^2-\alpha_3^2\right)\sin(2\theta)}{R^4\left(\alpha_0^2+\alpha_3^2\right)\epsilon}\left\{\frac{\epsilon r J_0\left(\frac{\epsilon r}{v}\right)-2vJ_1\left(\frac{\epsilon r}{v}\right)-\epsilon r J_2\left(\frac{\epsilon r}{v}\right)}{4r}\right\}. \tag{C6}$$

$$b_2(\mathbf{r}) = \frac{\alpha_0^2-\alpha_3^2}{2R^4\left(\alpha_0^2+\alpha_3^2\right)}\left\{J_0\left(\frac{\epsilon r}{v}\right)-\cos(2\theta)\frac{\left[\epsilon r J_0\left(\frac{\epsilon r}{v}\right)-2vJ_1\left(\frac{\epsilon r}{v}\right)-\epsilon r J_2\left(\frac{\epsilon r}{v}\right)\right]}{2\epsilon r}\right\}. \tag{C7}$$

$$b_3(\mathbf{r}) = \frac{2i\alpha_0\alpha_3\sin(\theta)J_1\left(\frac{\epsilon r}{v}\right)}{R^4\left(\alpha_0^2+\alpha_3^2\right)}. \tag{C8}$$

$$c_0(\mathbf{r}) = \frac{i\cos(\theta)J_1\left(\frac{\epsilon r}{v}\right)}{R^4\left(\alpha_0^2+\alpha_3^2\right)}. \tag{C9}$$

$$c_1(\mathbf{r}) = \frac{1}{2R^4\left(\alpha_0^2+\alpha_3^2\right)}\left\{J_0\left(\frac{\epsilon r}{v}\right)+\cos(2\theta)\frac{\left[\epsilon r J_0\left(\frac{\epsilon r}{v}\right)-2vJ_1\left(\frac{\epsilon r}{v}\right)-\epsilon r J_2\left(\frac{\epsilon r}{v}\right)\right]}{2\epsilon r}\right\}. \tag{C10}$$

$$c_2(\mathbf{r}) = \frac{1}{R^4\left(\alpha_0^2+\alpha_3^2\right)\epsilon}\left\{\sin(2\theta)\frac{\left[\epsilon r J_0\left(\frac{\epsilon r}{v}\right)-2vJ_1\left(\frac{\epsilon r}{v}\right)-\epsilon r J_2\left(\frac{\epsilon r}{v}\right)\right]}{4r}\right\}. \tag{C11}$$

APPENDIX D: COEFFICIENTS APPEARING IN THE PROPER VERTICES II: T MATRIX

$$\bar{a}_0(\mathbf{r}) = \frac{i(v+\delta v_{10})(\eta_+^2+\eta_-^2+\epsilon_+^2+\epsilon_-^2)\epsilon\cos(\theta)J_1\left(\frac{\epsilon r}{v}\right)}{4v^2(\eta_++\eta_-)}. \tag{D1}$$

$$\begin{aligned}\bar{a}_1(\mathbf{r}) = {}& \frac{(v+\delta v_{10})(\eta_+\eta_-+\epsilon_+\epsilon_-)}{4\epsilon v^2(\eta_++\eta_-)}\left\{\epsilon^2 J_0\left(\frac{\epsilon r}{v}\right)+\frac{\epsilon\cos(2\theta)\left[\epsilon r J_0\left(\frac{\epsilon r}{v}\right)-2vJ_1\left(\frac{\epsilon r}{v}\right)-\epsilon r J_2\left(\frac{\epsilon r}{v}\right)\right]}{2r}\right\}\\ &+\frac{\delta v_{20}(\eta_+\epsilon_--\eta_-\epsilon_+)}{4\epsilon v^2(\eta_++\eta_-)}\left\{\frac{\epsilon\cos(2\theta)\left[\epsilon r J_0\left(\frac{\epsilon r}{v}\right)-2vJ_1\left(\frac{\epsilon r}{v}\right)-\epsilon r J_2\left(\frac{\epsilon r}{v}\right)\right]}{2r}-\epsilon^2 J_0\left(\frac{\epsilon r}{v}\right)\right\}.\end{aligned} \tag{D2}$$

$$\bar{a}_2(\mathbf{r}) = \frac{\delta v_{20}(\eta_+\epsilon_--\eta_-\epsilon_+)+(v+\delta v_{10})(\eta_+\eta_-+\epsilon_+\epsilon_-)}{2v^2(\eta_++\eta_-)}\left\{\frac{\sin(2\theta)\left[\epsilon r J_0\left(\frac{\epsilon r}{v}\right)-2vJ_1\left(\frac{\epsilon r}{v}\right)-\epsilon r J_2\left(\frac{\epsilon r}{v}\right)\right]}{4r}\right\}. \tag{D3}$$

$$\bar{a}_3(\mathbf{r}) = \frac{i(v+\delta v_{10})(\eta_+^2-\eta_-^2+\epsilon_+^2-\epsilon_-^2)\epsilon\cos(\theta)J_1\left(\frac{\epsilon r}{v}\right)}{4v^2(\eta_++\eta_-)}. \tag{D4}$$

$$\bar{b}_0(\mathbf{r}) = \frac{i\delta v_{20}(\eta_+^2+\eta_-^2+\epsilon_+^2+\epsilon_-^2)\epsilon\sin(\theta)J_1\left(\frac{\epsilon r}{v}\right)}{4v^2(\eta_++\eta_-)}. \tag{D5}$$

$$\bar{b}_1(\mathbf{r}) = \frac{(v+\delta v_{10})(\eta_+\epsilon_--\eta_-\epsilon_+)-\delta v_{20}(\eta_+\eta_-+\epsilon_+\epsilon_-)}{2v^2(\eta_++\eta_-)}\left\{\frac{\sin(2\theta)\left[\epsilon r J_0\left(\frac{\epsilon r}{v}\right)-2vJ_1\left(\frac{\epsilon r}{v}\right)-\epsilon r J_2\left(\frac{\epsilon r}{v}\right)\right]}{4r}\right\}. \tag{D6}$$

$$\bar{b}_2(\mathbf{r}) = \frac{\delta v_{20}(\eta_+\eta_-+\epsilon_+\epsilon_-)+(v+\delta v_{10})(\eta_+\epsilon_--\eta_-\epsilon_+)}{4\epsilon v^2(\eta_++\eta_-)}\left\{\frac{\epsilon\cos(2\theta)\left[\epsilon r J_0\left(\frac{\epsilon r}{v}\right)-2vJ_1\left(\frac{\epsilon r}{v}\right)-\epsilon r J_2\left(\frac{\epsilon r}{v}\right)\right]}{2r}\epsilon^2 J_0\left(\frac{\epsilon r}{v}\right)\right\}. \tag{D7}$$

$$\bar{b}_3(\mathbf{r}) = \frac{i\delta v_{20}(\eta_+^2-\eta_-^2+\epsilon_+^2-\epsilon_-^2)\epsilon\sin(\theta)J_1\left(\frac{\epsilon r}{v}\right)}{4v^2(\eta_++\eta_-)}. \tag{D8}$$

[1] M. I. Dyakonov and V. I. Perel, JETP Lett. **13**, 467 (1971).

[2] J. E. Hirsch, Phys. Rev. Lett. **83**, 1834 (1999).

[3] S. Zhang, Phys. Rev. Lett. **85**, 393 (2000).

[4] Y. K. Kato, R. C. Myers, A. C. Gossard, and D. D. Awschalom, Science **306**, 1910 (2004); J. Wunderlich, B. Kaestner, J. Sinova, and T. Jungwirth, Phys. Rev. Lett. **94**, 047204 (2005).

[5] E. Saitoh, M. Ueda, H. Miyajima, and G. Tatara, Appl. Phys. Lett. **88**, 182509 (2006); S. O. Valenzuela and M. Tinkham, Nature (London) **442**, 176 (2006).

[6] L. Liu, T. Moriyama, D. C. Ralph, and R. A. Buhrman, Phys. Rev. Lett. **106**, 036601 (2011).

[7] K. Ando, S. Takahashi, K. Harii, K. Sasage, J. Ieda, S. Maekawa, and E. Saitoh, Phys. Rev. Lett. **101**, 036601 (2008).

[8] I. M. Miron, K. Garello, G. Gaudin, P.-J. Zermatten, M. V. Costache, S. Auffret, S. Bandiera, B. Rodmacq, A. Schuhl, and P. G. Bardella, Nature (London) **476**, 189 (2011); L. Liu, C.-F. Pai, Y. Li, H. W. Tseng, D. C. Ralph, and R. A. Buhrman, Science **336**, 555 (2012); L. Liu, O. J. Lee, T. J. Gudmundsen,

D. C. Ralph, and R. A. Buhrman, Phys. Rev. Lett. **109**, 096602 (2012).

[9] O. Mosendz, V. Vlaminck, J. E. Pearson, F. Y. Fradin, G. E. W. Bauer, S. D. Bader, and A. Hoffmann, Phys. Rev. B **82**, 214403 (2010); A. Azevedo, R. O. Cunha, F. Estrada, O. Alves Santos, J. B. S. Mendes, L. H. Vilela-Leão, R. L. Rodríguez-Suárez, and S. M. Rezende, *ibid.* **92**, 024402 (2015).

[10] K. Uchida, S. Takahashi, K. Harii, J. Ieda, W. Koshibae, K. Ando, S. Maekawa, and E. Saitoh, Nature (London) **455**, 778 (2010); K. Uchida, H. Adachi, T. An, T. Ota, M. Toda, B. Hillebrands, S. Maekawa, and E. Saitoh, Nat. Mater. **10**, 737 (2011); D. Qu, S. Y. Huang, J. Hu, R. Wu, and C. L. Chien, Phys. Rev. Lett. **110**, 067206 (2013).

[11] T. Tanaka, H. Kontani, M. Naito, T. Naito, D. S. Hirashima, K. Yamada, and J. Inoue, Phys. Rev. B **77**, 165117 (2008); H. L. Wang, C. H. Du, Y. Pu, R. Adur, P. C. Hammel, and F. Y. Yang, Phys. Rev. Lett. **112**, 197201 (2014).

[12] A. Fert and P. M. Levy, Phys. Rev. Lett. **106**, 157208 (2011); Y. Niimi, M. Morota, D. H. Wei, C. Deranlot, M. Basletic, A. Hamzic, A. Fert, and Y. Otani, *ibid.* **106**, 126601 (2011).

[13] M. Gradhand, D. V. Fedorov, P. Zahn, and I. Mertig, Phys. Rev. Lett. **104**, 186403 (2010).

[14] A. Ferreira, T. G. Rappoport, M. A. Cazalilla, and A. H. Castro Neto, Phys. Rev. Lett. **112**, 066601 (2014).

[15] A. A. Stabile, A. Ferreira, J. Li, N. M. R. Peres, and J. Zhu, Phys. Rev. B **92**, 121411(R) (2015).

[16] E. McCann and V. I. Fal'ko, Phys. Rev. Lett. **108**, 166606 (2012).

[17] A. Pachoud, A. Ferreira, B. Özyilmaz, and A. H. Castro Neto, Phys. Rev. B **90**, 035444 (2014).

[18] J. Balakrishnan, G. K. W. Koon, M. Jaiswal, A. H. Castro Neto, and B. Özyilmaz, Nat. Phys. **9**, 284 (2013).

[19] J. Balakrishnan, G. K. W. Koon, A. Avsar, Y. Ho, J. H. Lee, M. Jaiswal, S.-J. Baeck, J.-H. Ahn, A. Ferreira, M. A. Cazalilla, A. H. Castro Neto, and B. Ozyilmaz, Nat. Commun. **5**, 4748 (2014).

[20] Z. Wang, D.-K. Ki, H. Chen, H. Berger, A. H. MacDonald, and A. F. Morpurgo, Nat. Commun. **6**, 8339 (2015).

[21] F. Calleja, H. Ochoa, M. Garnica, S. Barja, J. J. Navarro, A. Black, M. M. Otrokov, E. V. Chulkov, A. Arnau, A. L. Vázquez de Parga, F. Guinea, and R. Miranda, Nat. Phys. **11**, 43 (2015).

[22] A. Avsar, J. Y. Tan, T. Taychatanapat, J. Balakrishnan, G. K. W. Koon, Y. Yeo, J. Lahiri, A. Carvalho, A. S. Rodin, E. C. T. O'Farrell, G. Eda, A. H. Castro Neto, and B. Ozyilmaz, Nat. Commun. **5**, 4875 (2014).

[23] H.-Y. Yang, C. Huang, H. Ochoa, and M. A. Cazalilla, Phys. Rev. B **93**, 085418 (2016).

[24] J. B. S. Mendes, O. Alves Santos, L. M. Meireles, R. G. Lacerda, L. H. Vilela-Leão, F. L. A. Machado, R. L. Rodríguez-Suárez, A. Azevedo, and S. M. Rezende, Phys. Rev. Lett. **115**, 226601 (2015).

[25] D. Huertas-Hernando, F. Guinea, and A. Brataas, Phys. Rev. B **74**, 155426 (2006).

[26] S. Konschuh, M. Gmitra, and J. Fabian, Phys. Rev. B **82**, 245412 (2010).

[27] T. Stauber, N. M. R. Peres, and F. Guinea, Phys. Rev. B **76**, 205423 (2007).

[28] J. P. Robinson, H. Schomerus, L. Oroszlany, and V. I. Fal'ko, Phys. Rev. Lett. **101**, 196803 (2008).

[29] T. O. Wehling, S. Yuan, A. I. Lichtenstein, A. K. Geim, and M. I. Katsnelson, Phys. Rev. Lett. **105**, 056802 (2010).

[30] A. Ferreira, J. Viana-Gomes, J. Nilsson, E. R. Mucciolo, N. M. R. Peres, and A. H. Castro Neto, Phys. Rev. B **83**, 165402 (2011).

[31] M. Milletarì, and A. Ferreira, arXiv:1601.08076.

[32] N. A. Sinitsyn, J. Phys. Condens. Matter **20**, 023201 (2008).

[33] N. A. Sinitsyn, Q. Niu, and A. H. MacDonald, Phys. Rev. B **73**, 075318 (2006).

[34] R. Raimondi, C. Gorini, P. Schwab, and M. Dzierzawa, Phys. Rev. B **74**, 035340 (2006).

[35] S. Irmer, T. Frank, S. Putz, M. Gmitra, D. Kochan, and J. Fabian, Phys. Rev. B **91**, 115141 (2015); R. M. G.- Arellano, A. D. H. Nieves, C. A. Balseiro, and G. Usaj, *ibid.* **91**, 195408 (2015).

[36] G. Baym, Phys. Rev. **127**, 1391 (1962).

[37] A. Ado, I. A. Dmitriev, P. M. Ostrovsky, and M. Titov, Europhys. Lett. **111**, 37004 (2015).

[38] E. I. Rashba, Phys. Rev. B **68**, 241315(R) (2003); S. Zhang and Z. Yang, Phys. Rev. Lett. **94**, 066602 (2005); J. Shi, P. Zhang, D. Xiao, and Q. Niu, *ibid.* **96**, 076604 (2006).

[39] A. Crepieux and P. Bruno, Phys. Rev. B **64**, 014416 (2001).

[40] J. Rammer, *Quantum Transport Theory*, Frontiers in Physics Vol. 99 (Westview Press, Boulder, 1998).

[41] P. J. Hirschfeld, P. Wölfle, and D. Einzel, Phys. Rev. B **37**, 83 (1988).

[42] T. S. Nunner, N. A. Sinitsyn, M. F. Borunda, V. K. Dugaev, A. A. Kovalev, A. Abanov, C. Timm, T. Jungwirth, J.-I. Inoue, A. H. MacDonald, and J. Sinova, Phys. Rev. B **76**, 235312 (2007).

[43] T. L. van den Berg, L. Raymond, and A. Verga, Phys. Rev. B **84**, 245210 (2011).

[44] A. Dyrdał and J. Barnas, Phys. Rev. B **86**, 161401(R) (2012).

[45] N. A. Sinitsyn, A. H. MacDonald, T. Jungwirth, V. K. Dugaev, and J. Sinova, Phys. Rev. B **75**, 045315 (2007).

[46] A. Zee, *Quantum Field Theory in a Nutshell*, 2nd ed. (Princeton University Press, Princeton, NJ, 2010).

[47] S. Murakami, N. Nagaosa, and S. C. Zhang, Phys. Rev. B **69**, 235206 (2004).

[48] A. Atland and B. Simons, *Condensed Matter Field Theory*, 2nd ed. (Cambridge University Press, Cambridge, 2010).

[49] H. Haug and A.-P. Jauho, *Quantum Kinetics in Transport and Optics of Semiconductors*, 2nd ed. (Springer, Berlin, 2010).

[50] J. Rammer, *Quantum Field Theory of Non-equilibrium States* (Cambridge University Press, Cambridge, 2007).

[51] NIST, NIST Digital Library of Mathematical Functions, http://dlmf.nist.gov/10.27.